

CENTRO BRASILEIRO DE PESQUISAS FÍSICAS

Grasiele Romanzini Bezerra

**IMPACT OF GALAXY DYNAMICS
ON MODIFIED GRAVITY
CONSTRAINTS FROM EINSTEIN
RINGS**

Rio de Janeiro (RJ), Brazil

July 2023

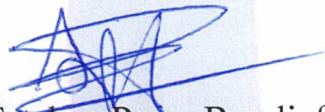
“IMPACT OF GALAXY DYNAMICS ON MODIFIED GRAVITY
CONSTRAINTS FROM EINSTEIN RINGS”

GRASIELE ROMANZINI BEZERRA

Dissertação de Mestrado em Física apresentada no
Centro Brasileiro de Pesquisas Físicas do
Ministério da Ciência Tecnologia e Inovação.
Fazendo parte da banca examinadora os seguintes
professores:



Martin Makler – Orientador/CBPF



Santiago Esteban Perez Bergliaffa - UERJ



Documento assinado digitalmente

DAVI CABRAL RODRIGUES

Data: 14/07/2023 08:32:18-0300

Verifique em <https://validar.iti.gov.br>

Davi Cabral Rodrigues – UFES

Rio de Janeiro, 07 de julho de 2023.

“IMPACT OF GALAXY DYNAMICS ON MODIFIED GRAVITY CONSTRAINTS FROM EINSTEIN RINGS”

Grasiele Romanzini Bezerra

Master's Dissertation presented at the Brazilian Center for Research in Physics of the Ministry of Science, Technology and Innovation as a partial requirement for obtaining the Master's degree in Physics.

Supervisor: Dr Martin Makler

Co-Supervisor: Dr Cristina Furlanetto

Dr Martin Makler - President/Supervisor/CBPF

Dr Santiago Esteban Perez Bergliaffa/UFRJ

Dr Davi Cabral Rodrigues/UFES

Rio de Janeiro (RJ), July 2023, Brazil

For all the women that came before me, their determination granted us access to science and education. And for all the women that will come after me, I hope that the world will treat you kindly.

We also know that many witches were midwives or “wise women”...

– Silvia Federici

The continuous process by which women were supplanted by men in the profession is one example of the way in which they were excluded from all branches of professional work, through being denied the opportunity of obtaining an adequate professional training.

– Alice Whitcomb Clark

Acknowledgments

First of all, I want to thank my amazing wife, Patricia Ternes, and our kitties, Fluidex Maria and Andromeda Maria, for being my solid ground and my rock throughout this journey.

I would also like to express my gratitude to my mother, Andreia Romanzini, my father, Marcio Farias Bezerra, and my grandmother, Lorena Elisia Romanzini, for their support in my life and education.

I am grateful to my siblings, Geovana Romanzini Bezerra, Alexander Romanzini Kuckert, Laura Anzanello Bezerra, and Antonio Romanzini Pires, for the healthy competition and for being such an integral part of my life and shaping who I am.

Special thanks to my supervisors, Martin Makler and Cristina Furlanetto, for their support in this work, their teaching, their ideas, and their patience.

I would like to express my appreciation to my psychologist, Maite Chika Carneiro, for helping me navigate through difficult times and preventing mental breakdowns.

I also want to express my gratitude to Gabriel Crisnejo and Renan Alves de Oliveira for have developed the *rings2cosmo* code which served as a crucial foundation for this project.

A special thanks to Mariana Penna Lima Vitenti for suggesting the use of the Cuba package for numerical integration. Her suggestions represented a vital turning point in this project.

To the Brazilian people, I am deeply grateful as I have studied in public institutions from the first grade to my master's degree, institutions that belong to and are supported by the people. The access to these institutions represents a significant social achievement for our country.

I extend my thanks to the Brazilian Center for Physics Research (CBPF) and its professors and staff for welcoming me during the Covid-19 pandemic. CBPF is not only the home of Brazilian physicists but also a reference in scientific research and technological advancements.

To all those mentioned above, I cannot express my gratitude enough.

Abstract

A test of General Relativity (GR) can be carried out using galaxy-galaxy Strong Lensing systems. In the weak field approximation, it is possible to characterise the space-time metric with two potentials: a Newtonian and a curvature one. The post-Newtonian parameter (γ_{PPN}) can be defined as the ratio of these two potentials and it is equal to one in GR. As gravitational lensing is sensitive to both potentials, while the stars kinematics of the lens galaxy are sensitive only to the Newtonian potential, the combination of these observables yields constraints on γ_{PPN} . The recent increase in the number of lens systems has reduced the statistical uncertainties of γ_{PPN} , however this method still presents some sources of systematic errors. Particularly, it is often assumed in the literature in this field that the anisotropy between the tangential and the radial components of the velocity dispersion of the stars in the lens galaxy, denoted by β , is constant. Furthermore, strong priors on β are usually set in the analyses that constrain γ_{PPN} with the combination of strong-lensing and galaxy dynamics. Our objective was to investigate the impact of the anisotropy parameter on the constraints on the γ_{PPN} , and to test if it is possible to constrain β and γ_{PPN} simultaneously. In this work we used a data set of 80 strong lensing systems from the BELLS, SLACS, LS2S and LSD surveys. We considered three classes of models for β . The first one has $\beta = \beta_0$ (constant) and we considered three sets of Gaussian priors on this quantity. We found that the data allows one to constrain γ_{PPN} , but the results depend on the prior. In particular, for high values of β_0 the result is in tension with GR. We also considered a flat prior in β_0 , which lead to very broad constraints on both $\gamma_{PPN,0}$ and β_0 . The second class refers to models where β has a radial dependence, with $\beta(r = 0) = 0$ and having a fixed asymptotic value at $r \rightarrow \infty$. A free parameter, a , controls the transition from the two regimes. In particular, we considered two radial profiles: the Osipkov-Merrit model (OM) and Mamon & Lokas model (ML). In these cases the data does not place strong constraints on a , but enables one to set constraints on γ_{PPN} , which peak at values below 1. Only at the 2.5σ level the results are consistent with GR. Finally, the third class is a generalisation of the ML model, adding an arbitrary normalisation β_0 to $\beta(r)$. As in the pure $\beta = \text{const.}$ model, we could not successfully constrain β_0 nor γ_{PPN} in this case. All models considered here have a similar goodness-of-fit to the data. This shows that adding complexity to the models does not improve the description of the current data. Therefore, the more parameters of the model, the less it is favoured by the data. Fixing the asymptotic behaviour of $\beta(r)$ or setting strong priors on β_0 sets rather strong constraints on γ_{PPN} , but they are incompatible with one another. In addition, we have seen that β_0 is strongly degenerate with γ_{PPN} , such that it is not possible to constrain them simultaneously from the data. We conclude that the choice of model and/or priors for β have a strong influence on the determination of γ_{PPN} .

Keywords: Strong Gravitational Lensing, Galaxy Dynamics, Modified Gravity

Resumo

Um teste da Relatividade Geral (RG) pode ser realizado usando sistemas de Lentes Gravitacionais Fortes (SL). Na aproximação do campo fraco, é possível caracterizar a métrica do espaço-tempo com dois potenciais: um newtoniano e um de curvatura. O parâmetro pós-newtoniano (γ_{PPN}) pode ser definido como a razão desses dois potenciais, e este é igual a um na RG. O lenteamento gravitacional é sensível a ambos os potenciais, enquanto a cinemática das estrelas da galáxia lente é sensível apenas ao potencial newtoniano, a combinação desses observáveis fornece restrições sobre γ_{PPN} . Este método apresenta algumas fontes de erros sistemáticos. Em particular, é frequentemente assumido na literatura dessa área que a anisotropia entre as componentes tangencial e radial da dispersão de velocidade das estrelas na galáxia lente, β , é constante. Além disso, são geralmente estabelecidas priors restritivos para β nas análises de γ_{PPN} . Nosso objetivo foi investigar o impacto do parâmetro de anisotropia nas restrições sobre γ_{PPN} e testar se é possível restringir β e γ_{PPN} simultaneamente. Neste trabalho, utilizamos um conjunto de dados de 80 sistemas de SL dos projetos BELLS, SLACS, LS2S e LSD. Consideramos três classes de modelos para β . A primeira tem $\beta = \beta_0$ (constante) e consideramos três conjuntos de priors Gaussianos para essa quantidade. Descobrimos que os dados permitem restringir γ_{PPN} , mas os resultados dependem do prior. Em particular, para valores altos de β_0 , o resultado apresentará tensão em relação a RG. Também consideramos um prior uniforme em β_0 , o que resultou em valores com altas dispersões tanto para $\gamma_{PPN,0}$ quanto para β_0 . A segunda classe refere-se a modelos onde β possui uma dependência radial, com $\beta(r = 0) = 0$ e um valor assintótico fixo em $r \rightarrow \infty$. O parâmetro livre a controla a transição entre os dois regimes. Em particular, consideramos dois perfis radiais: o modelo de Osipkov-Merritt (OM) e o modelo de Mamon & Lokas (ML). Nesses casos, os dados não impõem restrições fortes em a , mas permitem restringir γ_{PPN} , que resulta em valores abaixo de 1. Os resultados são consistentes com a RG apenas em 2.5σ . Finalmente, a terceira classe é uma generalização do modelo ML, no qual adicionasse um β_0 arbitrário a $\beta(r)$. Assim como no caso $\beta = \text{const.}$, não foi possível restringir com sucesso nem β_0 nem γ_{PPN} . Todos os modelos considerados aqui apresentam uma adequação semelhante aos dados. Isso mostra que adicionar complexidade aos modelos não melhora a descrição dos dados atuais. Portanto, quanto mais parâmetros no modelo, menos ele é favorecido pelos dados. Fixar o comportamento assintótico de $\beta(r)$ ou estabelecer priors restritivos para β_0 impõe restrições bastante fortes em γ_{PPN} , mas elas são incompatíveis entre si. Além disso, observamos que β_0 está fortemente degenerado com γ_{PPN} , de modo que não é possível restringi-los simultaneamente a partir dos dados. Concluímos que a escolha do modelo e/ou prior para β têm uma forte influência na determinação de γ_{PPN} .

Palavras-chave: Lentes Gravitacionais Fortes, Dinâmica de Galáxias, Gravidade Modificada

Contents

1	Introduction	1
1.1	Post-Newtonian Theory	3
1.2	Gravitational Lensing	4
1.3	Galaxy Dynamics	9
2	Methodology	14
2.1	Anisotropy parameter models	14
2.1.1	Constant Anisotropy Parameter β	16
2.1.2	Osipkov-Merritt Model	16
2.1.3	Mamon & Lokas Model	16
2.1.4	Generalised Tiert Model	18
2.2	Line-of-sight velocity dispersion and the observational conditions	18
2.3	Statistical Treatment	20
3	Results and Discussion	23
3.1	Data set	23
3.2	Results of the Markov Chain Monte Carlo Simulation	27
3.2.1	Constant Anisotropy Parameter β_0	27
3.2.2	Osipkov-Merritt Model	31
3.2.3	Mamon & Lokas Model	33
3.2.4	Generalised Tiert Model	34
3.3	Posterior Probability Density Function and Model Fitting	37
4	Conclusions and Future Work	41
A	Numerical Integration	51

List of Tables

- 3.1 The compilation of the Data Set used in this analysis. 26
- 3.2 The χ^2 for each model. 39
- 3.3 The Bayesian Information Criterion for each model. 40

List of Figures

1.1	The so called Horseshoe Einstein Ring from Hubble space Telescope.	5
1.2	Lensed arc in the system SDSS J120540.43+491029.3.	6
1.3	Strong Lens Systems Configuration.	7
1.4	Line-Of-Sight Projection Schema.	8
2.1	The radial behaviour of β profiles.	17
3.1	Some properties of the lenses in The data set.	27
3.2	Result of the Markov Chain Monte Carlo for the model with β constant and with a Gaussian prior.	28
3.3	Result of the Markov Chain Monte Carlo for the model with β constant and with a flat $P(\beta_0)$	29
3.4	Bivariate distribution of the free parameters β_0 and $\gamma_{PPN,0}$, for the model with β constant and with a flat $P(\beta_0)$	30
3.5	Result of the Markov Chain Monte Carlo for the Osipkov-Merritt Model for radial β	31
3.6	Bivariate distribution of the free parameters a and $\gamma_{PPN,OM}$, for the model with the Osipkov-Merritt profile for β	32
3.7	Result of the Markov Chain Monte Carlo for the Mamon & Lokas Model for radial β	33
3.8	Bivariate distribution of the free parameters a and $\gamma_{PPN,ML}$, for the model with the Mamon & Lokas profile for β	34
3.9	Result of the Markov Chain Monte Carlo for the Generalised Tired Model for radial β	35
3.10	Multivariate distribution of the free parameters β_0 , a and $\gamma_{PPN,GT}$, for the model with the Generalised Tired profile for radial β	36
3.11	Posterior Probability Distribution of γ_{PPN} for the models leading to Gaussian-like posterior PDFs for this quantity.	37
3.12	Posterior Probability Distribution for γ_{PPN} , for the models that yield a broad and skewed posterior for this parameter.	38

A.1	Typical values for $b = D_L \tilde{\sigma}_{atm}$.	54
A.2	Performance test for <code>scipy.integrate.dblquad</code> .	55
A.3	Performance test for GSL.	56
A.4	Performance test for <i>Cuba</i> .	57
A.5	Comparison of true errors across different routines for numerical integration.	58
A.6	Execution time test per ε_{rel}	58
A.7	Reproduction of the MCMC result for the model with β constant and with a flat $P(\beta_0)$.	59

List of Abbreviations

BELLS	BOSS Emission-Line Lens Survey
BIC	Bayesian Information Criteria
BOSS	Baryon Oscillation Spectroscopic Survey
CMB	Cosmic Microwave Background
ETG	Early-Type Galaxy
GPS	Global Positioning System
GR	General Relativity
GSL	GNU Scientific Library
GT	Generalised Tired Model
KDE	Kernel Density Estimator
LOS	Line Of Sight
LSD	Lenses Structure and Dynamics Survey
MCMC	Monte Carlo Markov Chain
ML	Mamon & Lokas Model
MLE	Maximum Likelihood Estimation
OM	Osipkov-Merritt Model
PDF	Probability Density Functions
PPN	Parametrized Post-Newtonian
QAG	Quadrature Adaptive Gaussian
SDSS	Sloan Digital Sky Survey

SIS Singular Isothermal Sphere
SL Strong Gravitational Lensing
SL2S Strong Lensing Legacy Survey
SLACS Sloan Lens Advanced Camera for Surveys

Chapter 1

Introduction

Albert Einstein's General Relativity (GR) Theory, published in 1915 [1, 2], remains the leading theory for describing gravitation. It has passed important tests within just a few years of its publication, including the correct prediction of variation in the Mercury's perihelion [3] and the solar eclipse of 1919 [4], which provided evidence for the bending of light in a gravitational field [5]. Over the last century, further studies have supported GR, such as the observation of relativistic effects in pulsars [6], which led to the Nobel Prize being awarded to Russell Hulse and Joseph Taylor in 1993¹, and the observed delay of photons passing through gravitational fields [7]. Additionally, understanding the relativistic nature of gravity was crucial for various technological advancements, including the Global Positioning System (GPS) [8].

In 2015, the detection of the gravitational waves [9, 10] opened a new window for the study of gravitation, leading to the 2017 Nobel Prize being awarded to Rainer Weiss, Barry Barish, and Kip Thorne². In the same year, the first detection of a gravitational wave produced by the inspiral of a neutron star occurred, which was followed up by the Fermi Gamma-Ray Burst Monitor [11]. This event, known as the kilonova *GW170817*, revolutionised the use of multi-messengers in the study of gravitation. More recently, the reconstruction of images of the shadow of the supermassive black hole in the centre of the galaxy M87 in 2019 [12] and the supermassive black hole Sgr A* at the centre of the Milky Way in 2022 [13] represent significant advancements in the field of General Relativity.

Notwithstanding the indisputable success of GR, specially at the solar system scales, there are still some mysteries when it comes to galactic and cosmological scales. For example, there is a large body of evidence that the Universe is in accelerated expansion [14]. To tackle this problem the concept of dark energy [15], an exotic element with negative pressure, was introduced. However, a discrepancy persists in the measuring of the rate of expansion, represented by the Hubble constant H_0 . Observations from the early Universe, such as the cosmic microwave

¹<https://nobelprize.org/prizes/physics/1993>

²<https://nobelprize.org/prizes/physics/2017>

background radiation (CMB), and those from the late Universe, such as type Ia supernovas, exhibit a tension of up to 5σ [16].

In addition to that, there is more matter than it is observed [17], for this case, the hypothesis of dark matter [18], a non-baryonic substance that makes most of the mass in galaxies and galaxy clusters, but does not interact with radiation, and therefore can not be seen was proposed. These two components (dark energy and dark matter) account for about 95% of the current matter-energy content of the Universe [19].

Alternatively, there are modified gravity theories that aim to solve these problems by altering the equations of motion, generally providing modifications to the GR Lagrangian. As for example chameleon gravity theories that seek to find solutions that decouple the relativistic effects in the solar system scale from the ones on cosmological scales [5, 20–22]. However, it is still unclear if modifying the gravity theories would be sufficient to explain the aforementioned cosmological phenomena without the aid of dark energy and dark matter. Therefore, further testing is required.

The parametrized post-Newtonian (PPN) framework is as a quantitative method for testing deviations from General Relativity. One of its key parameters, γ_{PPN} , quantifies the degree to which space-time bends under the influence of mass. Experimental studies on light-bending can constrain this parameter, which is expected to be equal to one in General Relativity [5, 21]. In this work we aim to measure the PPN parameter using data from strong gravitational lensing systems (SL) [23–29].

Strong gravitational lensing is the phenomena where the light of a distant source is deflected when by passing in the neighbourhood of a massive body, and forms multiple and/or highly distorted images of same object. When the lens is a galaxy, and there is adequate alignment between the source, the lens and the observer, the resulting images are arcs or, in some cases, complete rings. These configurations become collectively known as “Einstein Rings” [18, 30]. In the case where the lens is an Early-type galaxy (ETG), two observable quantities can be used as mass tracers for the lens: the relative angular position of the lensed image, known as Einstein radius, θ_E and the velocity dispersion of the stars in the galaxy, σ , which reflect the lensing effect and the stellar kinematics, respectively [31, 32].

It is possible to use strong gravitational lensing and kinematic data to constrain γ_{PPN} ; however, it is crucial to conduct a comprehensive investigation into the potential sources of systematic errors. In this study, our particular focus is on the error introduced by the challenging task of modelling the dynamics of the galaxy, which is manifested in the anisotropy of the velocity dispersion of the lens galaxy’s stars. This anisotropy is represented by the parameter β . The majority of previous studies in this field commonly assume a constant value for the anisotropy parameter [23, 33–35]. The main challenge lies in constraining this parameter since it cannot be directly measured through observations. Nevertheless, existing literature on galaxy

dynamics suggests that the anisotropy parameter should exhibit a radial dependence [32, 35].

The primary objective of this work is to explore the interplay between the modelling the anisotropy in the velocity dispersion of the stars of the lens galaxy and the constraints on the post-Newtonian parameter in Einstein Ring systems. In particular, we aim to investigate the impact of radially dependent anisotropy parameters, $\beta = \beta(r)$, using three different models: the Osipkov-Merritt model [36, 37], the Mamon & Lokas model [35], and the Generalized Tirret model [38, 39]. By comparing these different models with the results for constant β , we aim to gain insights into the influence of anisotropy on the determination of γ_{PPN} .

This text is organised as follows: In the next three sections we will delve into the three main concepts that are the building blocks of this work: the post-Newtonian Theory, strong gravitational lensing and galaxy dynamics. Subsequently, in Chapter 2, we will outline the methodology by presenting the models for β that are used in this work, discussing the comparison with observational data, and describing the statistical treatment applied. In Chapter 3 we aim to present the data set used and the results obtained. Finally, in Chapter 4 we will summarise our conclusions and main insights that outcome from this study.

1.1 Post-Newtonian Theory

The post-Newtonian Theory arose in the previous century as a way to impose Newtonian limit to slow moving bodies under weak gravitational fields [40]. Its metric is written as an expansion in terms of the gravitational potential centred around the Minkowskian metric. Furthermore, this metric can also be parametrized with the objective of performing physical tests, resulting in the parametrized post-Newtonian (PPN) formalism. In this work, we will use the PPN metric to the first-order expansion, given by [5, 21]

$$g_{00}^{PPN} = -1 + 2\frac{GM}{r}, \quad (1.1a)$$

$$g_{0i}^{PPN} = 0, \quad (1.1b)$$

$$g_{ij}^{PPN} = \left(1 + 2\gamma_{PPN}\frac{GM}{r}\right)\delta_{ij}, \quad (1.1c)$$

where G is the universal gravitational constant, M is the mass curving the space-time, r is the distance to the body's centre of mass, and γ_{PPN} is the PPN parameter that measures how much the space-time bend for unity of mass.

This particular post-Newtonian parameter can be constrained using the bending of the light in curved space-time, and therefore, it is crucial for experiments involving gravitational lensing. However it is not the only PPN parameter, for other experiments, as for example the measurement of the precession on the perihelion of Mercury, one might need a second order

expansion of the PPN metric, which will be associated to a second PPN parameter [5, 21, 41]. Additionally, it is important to state that for this work we will assume a particular GR modification in which γ_{PPN} is constant, if one wishes to consider other modifications it might be necessary review the metric [20, 22, 42, 43]. The post Newtonian formalism can have an infinite number of parameters, but in reference [5] it is discussed the first 10 of them.

In addition to that, in the weak field limit, it is often convenient to describe the metric of space-time in terms of a Newtonian potential Φ and a curvature potential Ψ . This allows us to express the comoving distance element ds^2 as [26]:

$$ds^2 = a^2(\tau)[-(1 + 2\Phi)d\tau^2 + (1 - 2\Psi)\sigma_{ij}dx^i dx^j] \quad (1.2)$$

Here, τ represents the proper time coordinate, x^i corresponds to the spatial coordinate, and σ_{ij} is the spatial components of the metric in a space with constant curvature [44]. This formulation enables us to define the slip η as the ratio of the two potentials [41]:

$$\eta \equiv \frac{\Psi}{\Phi}. \quad (1.3)$$

For the metric on Equations (1.1) one can write the above potentials as

$$\Phi = \frac{GM}{r}, \quad (1.4a)$$

$$\Psi = \gamma_{PPN} \frac{GM}{r}. \quad (1.4b)$$

Altogether, when using Equation (1.4) on Equation (1.3) it is possible to show that for this particular case $\eta|_{PPN} = \gamma_{PPN}$. That is the reason why γ_{PPN} is often referred to in the literature as the ratio between the metric potentials [24–26]. Nonetheless, this statement is true only in the aforementioned case [41].

In summary, the parametrized post-Newtonian framework provides us with useful tools to test gravity. Gravitational lensing is sensitive to both potentials ($\Phi + \Psi$), while the stellar kinematics of the lens galaxy exclusively relates to the Newtonian potential (Φ). By combining these observables, we can effectively constrain the parameter γ_{PPN} . In the next section we will discuss the lens equation under this formalism.

1.2 Gravitational Lensing

Gravitational lensing is the phenomenon in which the light of a distant source is deflected when passing by a gravitational field. Some consequences of this deflection are the deformation of the source image (due to the lensing magnification), the appearance of multiple images and

the time delay between images. It has several astrophysical applications, as for example the observation of sources that would not be visible otherwise, the study of dark matter in clusters (e.g. [31, 45, 46]), and, as will be discussed in this work, the study of the mass distribution of the galaxies acting as lenses [47] and constraints on gravitation and cosmological theories [23–28, 48].

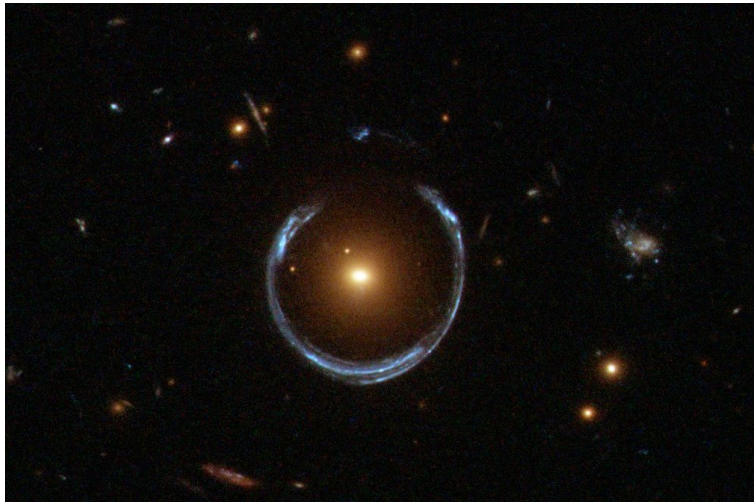


Figure 1.1: The so called Horseshoe Einstein Ring from Hubble space Telescope. Image Credit: ESA/Hubble & NASA

As a means to constrain the γ_{PPN} parameter, as discussed on the previous section, we shall consider strong lensing systems in which the lens is an ETG and there is nearly perfect alignment between source, lens and observer. In these systems, the images of the source can take the form of complete rings, as illustrated in Figure 1.1, or more commonly, arcs, as depicted in Figure 1.2. Although the SL systems utilised in this study exhibit more arc-like structures rather than rings, these structures are commonly referred to as Einstein rings. These formations can be modelled to determine a measure of the lensed image’s relative position, known as the Einstein radius, denoted by θ_E .

In order to obtain the lens mass using the lensing effect one needs to solve the Lens equation. Consider the system configuration illustrated in Figure 1.3: the red circle (S) represents the source with an angular position θ_S in the sky plane, the yellow circle represents the lens aligned with the observer along the line of sight (Z -axis), and the blue circles depict the potential images formed when the source’s light passes through the lens. The angular position of the images is denoted by θ_I , and the deflection angle is represented by α .

The reduced deflection angle, α , in Figure 1.3, is a function of the angular position of the image, θ_I , scaled by the cosmological distances between the observer and source (D_S) and

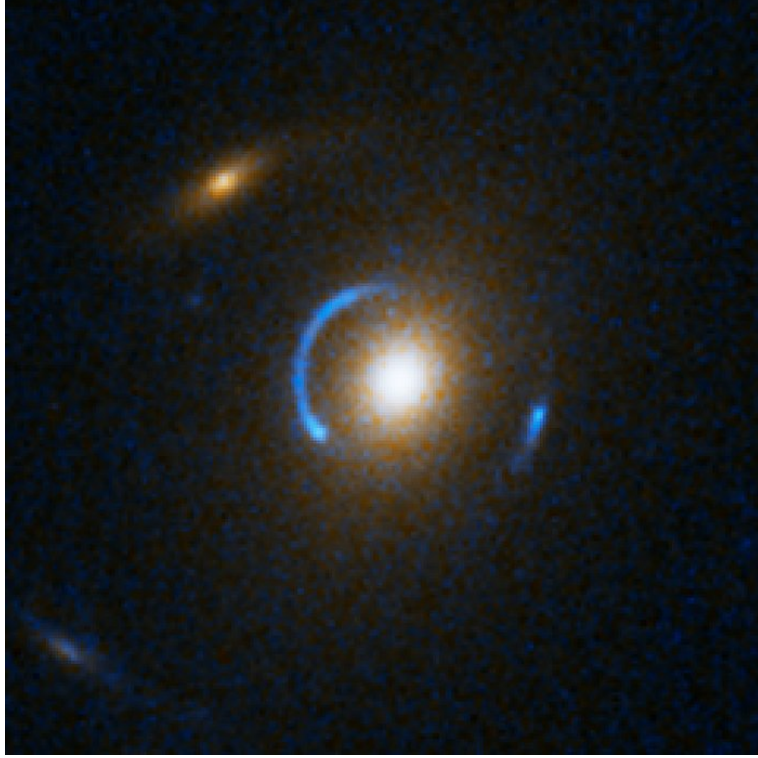


Figure 1.2: Lensed arc in the system SDSS J120540.43+491029.3. Image Credit: NASA, ESA, A. Bolton (Harvard-Smithsonian CfA) and the SLACS Team

between the lens and source (D_{LS}). It can be obtained through the following equation [18]:

$$\alpha(\theta_I) = \frac{D_{LS}}{D_S} \hat{\alpha}(R), \quad (1.5)$$

where $\hat{\alpha}(R)$ represents the deflection angle as a function of the physical position of the image in the lens plane, denoted by R . Since the angles involved are relatively small, we can relate the physical position to the angular position using $R = D_L \theta$, where D_L is the cosmological distance between the observer and lens. For this configuration, the lens equation is given by:

$$\theta_S = \theta_I - \alpha(\theta_I). \quad (1.6)$$

Along with this, the deflection angle can be calculated as follow [30]

$$\hat{\alpha} = \frac{2}{c^2} \int_{-\infty}^{\infty} \nabla_{\perp} \tilde{\Psi}_L dZ, \quad (1.7)$$

where $\tilde{\Psi}_L$ is the lens' potential and $\nabla_{\perp} \tilde{\Psi}_L$ is the projection of $\nabla \tilde{\Psi}_L$ on the plane of the lens (orthogonal to the line of sight) and can be calculated as $\nabla_{\perp} \tilde{\Psi}_L = \nabla \tilde{\Psi}_L - \hat{k}(\hat{k} \cdot \nabla \tilde{\Psi}_L)$.

In the previous section we defined the space-time metric in terms of two potentials, a Newtonian potential Φ , and a curvature potential Ψ . The lens effect is sensitive to both

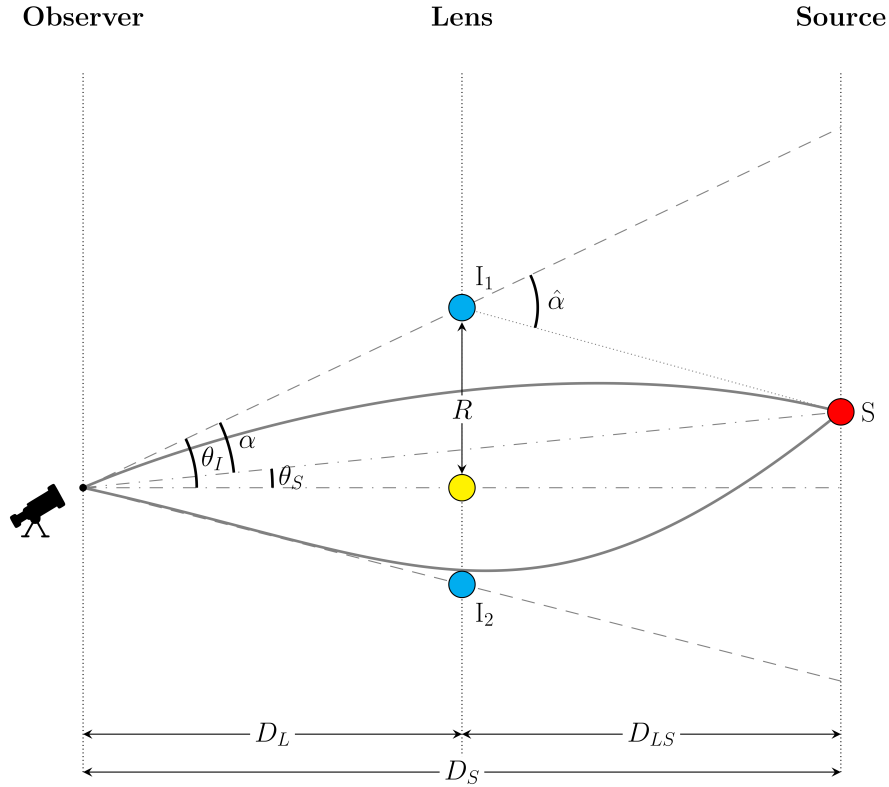


Figure 1.3: Strong Lens Systems Configuration.

potentials, therefore one must use the potentials on Equation (1.4) to find the lens potential as in [21]

$$\tilde{\Psi}_L = \frac{1}{2}(\Phi + \Psi) = -\frac{1 + \gamma_{PPN}}{2} \frac{GM}{r}, \quad (1.8)$$

where M is the mass of the lens. Subsequently, one can replace the lens potential in Equation (1.8) on Equation (1.7) and obtain the deflection angle as

$$\hat{\alpha}(R) = (1 + \gamma_{PPN}) \frac{2}{c^2} \frac{GM}{R} \hat{R}. \quad (1.9)$$

In order to solve the lens Equation (1.6) for the Einstein ring, one must express the deflection angle as a function of the image position $\hat{\alpha}(R_E)$, where $R_E = D_L \theta_E$ is the physical Einstein radius. Additionally, as we are considering systems that have nearly perfect alignment between source, lens and observer, we have that $\theta_S \approx 0$. Finally, by replacing this on Equation (1.6) one can obtain an equation for the Einstein radius in terms of γ_{PPN}

$$\theta_E = \sqrt{\frac{1 + \gamma_{PPN}}{2}} \left(\frac{4GM}{c^2} \frac{D_{LS}}{D_L D_S} \right)^{1/2}, \quad (1.10)$$

where M is the mass of the lens, which deforms the space-time and causes the deflection of the source light. Because of that, it will be referred to as lensing mass and it will be denoted as

M_E , from now on.

In order to calculate the lensing mass, one can integrate the surface mass density of the lens $\Sigma(R)$ from the centre of the lens up to the Einstein ring, i.e the mass enclosed by a cylinder with radius equal to the Einstein radius, as illustrated in Figure 1.4(a). In such case, the three-dimensional density, ρ , can be projected onto the plane of the sky by integrating it along the line of sight (LOS), perpendicular to the sky's plane, as shown in Figure 1.4(b). This density profile, as we will demonstrate in the next section, can be approximated by a power law, as given in Equation (1.22). With this we can obtain the surface density as

$$\Sigma(R) = \int_{-\infty}^{\infty} \rho(r) dZ = \frac{\rho_0}{r_0^{1-\alpha}} R^{1-\alpha} B\left(\frac{\alpha-1}{2}, \frac{1}{2}\right), \quad (1.11)$$

where B is the beta function. And following that, the lensing mass will be giving by

$$M_E = \int_S \Sigma(R) d\mathbf{x}^2 = 2\pi \frac{\rho_0}{r_0^{1-\alpha}} \sqrt{\pi} \lambda(\alpha) \frac{R_E^{3-\alpha}}{3-\alpha}, \quad (1.12)$$

where $\lambda(\alpha) = \Gamma\left(\frac{\alpha-1}{2}\right) / \Gamma\left(\frac{\alpha}{2}\right)$, and Γ is the gamma function.

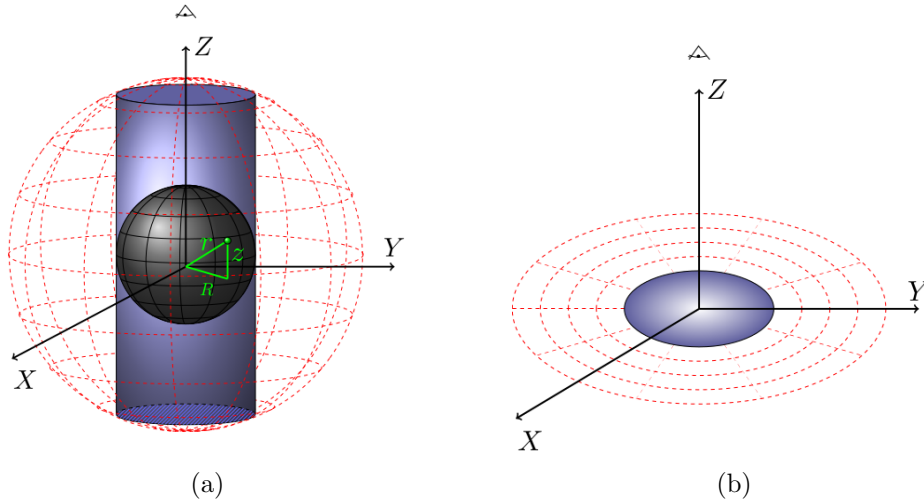


Figure 1.4: Mass distribution (a) on a cylinder and a sphere and (b) the projection in the plane perpendicular to the line of sight

In this section, we obtained an expression for the Einstein radius in terms of the post-Newtonian parameter γ_{PPN} by solving the lens equation. Alongside with that, we have calculated the lensing mass of the galaxy acting as lens. In the next section we will explore the kinematics of the stars in the lens galaxy.

1.3 Galaxy Dynamics

In the previous section, we show that in strong lensing systems, a nearly spherical lens can cause the source's image to form arcs. ETGs provide examples of such lenses. These are massive elliptical galaxies that have little gas and, consequently, little star formation [32, 33, 49, 50]. In general, their dynamics is dominated by the stellar velocity dispersion, which serves as the primary indicator of their dynamical mass. The dynamics of ETGs can be described by the Newtonian potential showed in Equation (1.4a).

As discussed in [32], it is impossible to follow each individual orbit of the stars in elliptical galaxies. A more reasonable approach is to work with the probability $f(\mathbf{x}, \mathbf{v}, t)d\mathbf{x}d\mathbf{v}$ of finding a star in a position \mathbf{x} with velocity \mathbf{v} at a given the time t . Defining such a probability distribution function is challenging, and $f(\mathbf{x}, \mathbf{v}, t)$ can not be measured directly from observational data. Therefore, we will explore the concept of a probability distribution to derive more practical observables.

Following the concept of probability distribution function, one can define the star density function as the probability to find a star regardless it velocity,

$$\nu(\mathbf{x}) \equiv \int d^3\mathbf{v} f(\mathbf{x}, \mathbf{v}, t). \quad (1.13)$$

As mentioned before, ETGs have a minimal amount of gas, consequently, their stars are responsible for the most of the mass of luminous matter. Therefore, it is reasonable to consider $\nu(\mathbf{x})$ approximately equal to the brightness profile.

Having elucidated that, we can now define the stellar velocity dispersion tensor

$$\sigma_{ij}^2 = \frac{1}{\nu(\mathbf{x})} \int d^3\mathbf{v} (v_i - \bar{v}_i)(v_j - \bar{v}_j) f(\mathbf{x}, \mathbf{v}, t) = \overline{v_i v_j} - \bar{v}_i \bar{v}_j, \quad (1.14)$$

where \bar{v}_i is the mean velocity component i , obtained by doing

$$\bar{v}_i = \frac{1}{\nu(\mathbf{x})} \int d^3\mathbf{v} v_i f(\mathbf{x}, \mathbf{v}, t). \quad (1.15)$$

In the case of a nearly spherical system, it is possible to select a coordinate system where the velocity dispersion tensor is diagonal, as a result, σ_{ij}^2 is zero when $i \neq j$.

The velocity dispersion discussed above can be associated with the one measured through the electromagnetic spectra of the galaxy, however, Equation (1.14) still depends on the probability distribution function. In order to calculate the velocity dispersion, we are going to use the approach presented in the Chapter 4 of [32]. With that in mind, if each star of the system has a Hamiltonian like

$$H = \frac{1}{2}v^2 + \Phi(\mathbf{x}), \quad (1.16)$$

where v is the velocity of the star and $\Phi(\mathbf{x})$ is the (Newtonian) potential, then one can use the Hamilton equation to write the collisionless Boltzmann equation as

$$\frac{\partial f}{\partial t} + \mathbf{v} \cdot \frac{\partial f}{\partial \mathbf{x}} - \frac{\partial \Phi}{\partial \mathbf{x}} \cdot \frac{\partial f}{\partial \mathbf{v}} = 0. \quad (1.17)$$

To solve Equation (1.17) one can make use of the spherical symmetry and write it on spherical coordinates

$$\begin{aligned} & \frac{\partial f}{\partial t} + v_r \frac{\partial f}{\partial r} + \frac{v_\theta}{r} \frac{\partial f}{\partial \theta} + \frac{v_\phi}{r \sin \theta} \frac{\partial f}{\partial \phi} \\ & - \left(\frac{\partial \Phi}{\partial r} - \frac{v_\theta^2}{r} - \frac{v_\phi^2}{r} \right) \frac{\partial f}{\partial v_r} - \left(\frac{\partial \Phi}{\partial \theta} - v_\phi^2 \cos \theta \right) \frac{1}{r} \frac{\partial f}{\partial v_\theta} - \frac{1}{r \sin \theta} \frac{\partial \Phi}{\partial \phi} \frac{\partial f}{\partial v_\phi} = 0, \end{aligned} \quad (1.18)$$

First, we are looking for a stationary solution. Therefore the term $\partial f / \partial t$ is equal to zero. Secondly, as we are consider spherical symmetry, we can eliminate any derivative in terms of angular coordinates. The next step is to integrate Equation (1.18) over the velocity phase space, using the Green theorem to keep the partial derivatives. Finally, by using Equation (1.15) we obtain the so called *Jeans Equation* [32]

$$\frac{\partial(\overline{\nu v_r^2})}{\partial r} + \frac{\nu}{r} \left(2\overline{v_r^2} - \overline{v_\theta^2} - \overline{v_\phi^2} \right) = -\nu \frac{d\Phi}{dr}. \quad (1.19)$$

For stationary systems, the average velocity components \bar{v}_i vanish [51]. In this context, it is valid to express the radial component of the velocity dispersion tensor as $\sigma_{ii}^2 = \overline{v_i^2}$, meaning that $\overline{v_r^2} = \sigma_r^2$. Additionally, the second moments of the angular components of the velocity are equal, implying that $\overline{v_\theta^2} = \overline{v_\phi^2} = \sigma_r^2$. The relationship between σ_r^2 and σ_τ^2 can be summarised by the anisotropy parameter β , defined as:

$$\beta \equiv 1 - \frac{\overline{v_\theta^2} + \overline{v_\phi^2}}{2\overline{v_r^2}} = 1 - \frac{\sigma_\tau^2}{\sigma_r^2}. \quad (1.20)$$

This parameter measures the anisotropy between the radial and tangential velocity dispersion. By definition its values are in the range $[-\infty, 1]$. When $\beta = 0$ the galaxy is an isotropic system, when $\beta < 0$ the tangential component of the velocity dispersion of the stars is privileged, when $\beta > 0$ the stars velocities are radially biased. The parameter β can not be measured directly by observations [50, 51], but there are works in the literature that discuss models for it [35–39, 52]. In this work we intend to address to what extent different models for β can affect the measurement of the post-Newtonian parameter described in Section 1.1.

Earlier works on N-body simulations for galaxy dynamics suggest that, for ETGs, β should be nearly zero close to the centre of the galaxy an increase monotonically with the radius [32]. Most recent publications in the matter use the magneto-hydrodynamic cosmological simulations

project *IllustrisTNG* [33, 49–51]. In these series of papers they conclude again that galaxies that have less internal gas and are at lower redshifts tend to have higher radial anisotropy, while galaxies with more gas and at higher redshifts tend to be more tangentially biased. Because the ETGs are represented by the first group, the condition $\beta > 0$, will be often used in this work. In reference [33] they obtained a mean value $\langle\beta\rangle = 0.23 \pm 0.19$ for a simulated ETGs' sample.

To solve the right side of Equation (1.19), it is possible to use the expression

$$\frac{d\Phi}{dr} = \frac{GM(r)}{r^2}, \quad (1.21)$$

where $M(r)$ is the total mass (accountable by the visible and dark matter) of the galaxy enclosed within a radius r from the galaxy centre. This mass will be referred to as dynamical mass and will be denoted as $M_{\text{dyn}}(r)$. This quantity is obtained by integrating the mass density profile ρ over the volume of the galaxy up to radius r . For the case of the ETGs, ρ can be well approximated by a power law [32]

$$\rho(r) = \rho_0 \left(\frac{r}{r_0}\right)^{-\alpha}. \quad (1.22)$$

where ρ_0 and r_0 are proportionality constants for the density and radius respectively and α is the adjustable slope.

In the particular case in which α is equal to two, it corresponds to a singular isothermal sphere (SIS), a self-gravitating ideal gas in equilibrium. Observational evidence has shown that this is a good approximation to the total density profile of the Early-type galaxies [53–56]. This is despite the fact that neither dark matter nor stars, the main components responsible for the mass of ETGs, present such behaviour. This phenomena is known as the “bulge-halo conspiracy”. The *IllustrisTNG* simulations has confirmed the SIS-like density profile for ETGs, with a measured average value of $\langle\alpha\rangle = 2.01 \pm 0.17$ in the simulated sample [33]. In addition to that, it has found that the slope value is nearly constant for $z < 1$, and then shows a slight increase with increasing redshift [33, 51]. In this work, we will let α be a free parameter, but we will impose a Gaussian prior centred around the SIS value. The details of this will be discussed on Section 2.3.

For the power law in Equation (1.22), the dynamical mass is given by

$$M_{\text{dyn}}(r) = \int_V \rho(r) d\mathbf{x}^3 = \frac{4\pi\rho_0}{r_0^{-\alpha}} \frac{r^{3-\alpha}}{3-\alpha}. \quad (1.23)$$

Then, we can eliminate the proportionality constants ρ_0 and r_0 by using Equation (1.12)

$$M(r) = \frac{2}{\sqrt{\pi}\lambda(\alpha)} \left(\frac{r}{R_E} \right)^{3-\alpha} M_E. \quad (1.24)$$

This approach provides a means to compare the lensing effects with the galactic dynamics.

All things considered, we can now move on to solving the Jeans Equation. By using Equations (1.20) and (1.21), we can rewrite the Jeans Equation (1.19) in a more commonly used form found in recent literature [25]

$$\frac{d(\nu\sigma_r^2)}{dr} + \frac{2\beta(r)}{r}\nu(r)\sigma_r^2(r) = -\nu(r)\frac{GM(r)}{r^2}. \quad (1.25)$$

As shown in [35], a general solution for this equation is given by

$$\nu(r)\sigma_r^2(r) = \frac{1}{f(r)} \int_r^\infty f(r')\nu(r')\frac{GM(r')}{r'^2}dr', \quad (1.26)$$

where $f(r)$ represents the solution for the differential equation

$$\frac{d \ln f}{d \ln r} = 2\beta(r). \quad (1.27)$$

This equation can be solved using the following approach

$$f(r) = f(r_1) \exp \left[\int_{r_1}^r 2\beta(r')\frac{dr'}{r'} \right], \quad (1.28)$$

with r_1 being an arbitrary reference radius.

The combination of SL and galaxy dynamics to constraint the post-Newtonian parameter was used in 2006 by [23], where it was obtained $\gamma_{PPN} = 0.98 \pm 0.07$ in a sample of 15 strong lensing systems. Later, in 2010, [24] used 53 Einstein rings systems to constrain the PPN parameter and the result was $\gamma_{PPN} = 1.01 \pm 0.05$. In this same work it was shown that this methodology can also be used to constrain cosmological parameters, such as the dark energy density fraction Ω_Λ , for which they obtained $\Omega_\Lambda = 0.75 \pm 0.17$. The systematical errors in the modelling of the lens galaxy dynamics were also evaluated in this reference. It was argued that there are three main sources for such systematical errors. First the mas density profile shape, which can be approximated by a power law with the slope α , considered a free parameter. In the case of ETGs, α is approximately to 2, that is the value for a singular isothermal sphere (SIS) [32]. Second there is the light density profile shape, for which it also considered a power law with adjustable slope δ and the value $\delta = 2.40 \pm 0.11$ was used. And finally, the anisotropy between the radial and tangential components of the stellar velocity dispersion, encoded in the parameter β , is extremely difficult to quantify, consequently, β is also a source of systematic.

The main conclusion of that work is that the systematical errors are comparable to the statistical ones, and therefore this analysis is limited by it.

Subsequently, in [25] the PPN parameter was constrained with 80 SL systems and the result was $\gamma_{PPN} = 0.995^{+0.037}_{-0.047}$. In that paper it was also proposed to impose a prior on the space-time curvature parameter Ω_k , the matter density fraction Ω_m and dark energy state equation ω , and with that it was found that $\gamma_{PPN} = 1.0000^{+0.0023}_{-0.0025}$. The systematic errors caused by α , δ and β were estimated to account for an uncertainty of $\sim 25\%$. In the following year the paper [26] was published, where they model the Einstein ring system *ESO325-G004*. The velocity dispersion for this system was measured pixel by pixel, which allowed them to define a very precise model for the lens' dynamics. They found that $\gamma_{PPN} = 0.97 \pm 0.09$.

Recently, in the work of reference [27], a sample of 120 systems, from the compilation provided by [48], was used to measure γ_{PPN} , and for this, three models for the slope of the mass density profile of the lens galaxy were considered. First it was considered to be constant but constrained by a prior centred in 2, with this they obtained $\gamma_{PPN} = 1.179^{+0.081}_{-0.096}$. The second model was a parameterization in which α depends on the redshift of the lens, and it resulted in $\gamma_{PPN} = 1.455^{+0.154}_{-0.127}$. Finally, a model for which α is a function of the redshift and the surface mass density of the lens galaxy was considered, and with that it was obtained $\gamma_{PPN} = 1.065^{+0.064}_{-0.074}$. In terms of the slope of the mass density, we are going to discuss later that recent works on ETG's dynamics has shown that α is constant and close to 2 when $z_L < 1$, then it increases steadily with the redshift [33, 49, 50], and because of that we are going to use the first model for this dissertation.

Last but not least, in [28] the degeneracy between post-Newtonian parameter and the curvature parameter was studied. With the same 120 SL systems cited above, they measured $\gamma_{PPN} = 1.11^{+0.11}_{-0.09}$ and $\Omega_k = 0.48^{+1.09}_{-0.71}$. They also obtained $\gamma_{PPN} = 1.07 \pm 0.07$ when Ω_k is fixed in zero, and $\Omega_k = 0.12^{+0.48}_{-0.36}$ when γ_{PPN} is fixed in 1. It is also interesting to mention the paper [48], in which they used a similar methodology, however instead of γ_{PPN} , they measured Ω_m , and with that it was demonstrated how flexible Einstein rings system are for probing cosmological models.

All aforementioned works assumed a constant profile for β . In the next chapter we are going to solve Equation (1.25) for different models for the anisotropy in the velocity dispersion of the stars in the lens galaxy.

Chapter 2

Methodology

In this chapter we will dive further into models and procedures employed in this study to address the research objectives. Section 2.1 presents the models of anisotropy between the radial and tangential components of velocity dispersion of the stars in the lens galaxy that will be used in this work. In addition to that, we solve the Jeans Equation (1.25) to obtain the radial component for each case. Following that, in Section 2.2 we discuss how these results can be related to the observational data. Finally, in Section 2.3, we derive the statistical framework used in this analysis to fit the model to the data.

2.1 Anisotropy parameter models

One of the most challenging unknowns of the Jeans Equation (1.25) is the parameter that measures the anisotropy between the radial and the tangential components of the velocity dispersion of the stars in the lens galaxy, β . It cannot be directly measured through observation [50] and inaccurate assumptions about this parameter can introduce biases on other galactic properties [51]. A simple solution for Equation (1.26) is obtained by assuming a constant value for β , this is one of the reasons why this approach is the most commonly used [23–25, 27, 28, 48]. However, previous studies in galaxy dynamics suggest that β should increase with the radius r of the galaxy [32, 33, 35].

In this section, we explore models with radially varying β . The radial dependence is commonly parameterised as [52]

$$\beta(r) = \beta_0 + \beta_1 \frac{r^n}{r^n + r_a^n}. \quad (2.1)$$

Here, β_0 represents the value of $\beta(r)$ when $r = 0$, while β_1 is determined by $\beta_1 = \beta_\infty - \beta_0$, with β_∞ denoting the asymptotic behaviour of the anisotropy profile as r tends to infinity, and n is the slope that controls the sharpness of the anisotropy profile. Additionally, r_a is a characteristic radius defined in terms of the dimensionless parameter a and r_{200} , given by

$r_a \equiv ar_{200}$. Here, r_{200} is defined as the radius at which the mean density of the galaxy equals 200 times the present critical density of the Universe, denoted as ρ_{crit} and it is obtained through [32]

$$\rho_{crit} = \frac{3H_0^2}{8\pi G}, \quad (2.2)$$

where H_0 is the Hubble constant [19].

As it is difficult to define an exact radius for the galaxies, it is common to consider r_{200} as a typical radius. In order to calculate it one can consider a sphere with homogeneous density $\rho_{200} = \Delta\rho_{crit}$, where $\Delta = 200$, and therefore the mass will be given by

$$M_{200} = \frac{4}{3}\pi r_{200}^3 \rho_{200}. \quad (2.3)$$

On the other hand, one can use Equation (1.24) and obtain $M(r_{200}) = M_{200}$. When applied to Equations (2.2) and (2.3), r_{200} can be expressed as

$$r_{200} = \left(\frac{2\mu}{\Delta H_0^2} \right)^{1/\alpha} \quad (2.4)$$

where μ incorporates the parameters from Equations (1.10) and (1.24), and is

$$\mu \equiv \frac{1}{1+\gamma} \frac{c^2}{\sqrt{\pi}\lambda(\alpha)} \frac{D_S}{D_{LS}} \frac{D_L^{\alpha-2}}{\theta_E^{1-\alpha}}. \quad (2.5)$$

For the parameterisation in Equation (2.1), the $f(r)$ function in Equation (1.28) takes the form

$$f(r) = (r^n + r_a^n)^{\frac{2\beta_1}{n}} r^{2\beta_0}. \quad (2.6)$$

Notwithstanding the analytical intractability of solving Equation (1.26) with this particular $f(r)$ function, simple solutions can be obtained for fixed values for the parameters n , β_0 , and β_∞ . In the following sections, we will explore several examples of β profiles with fixed parameters found in the literature. Additionally, we will determine the corresponding solutions for the Jeans Equation by assuming a power-law form for the brightness profile $\nu(r)$

$$\nu(r) = \nu_0 \left(\frac{r}{r_0} \right)^{-\delta}, \quad (2.7)$$

where δ is the adjustable slope, while ν_0 and r_0 serve as reference values [24, 32].

2.1.1 Constant Anisotropy Parameter β

When the objective is to test the General Relativity (GR) by combining strong lensing and kinematical data, the most common solution for Equation (1.25) is to use a constant anisotropy parameter, $\beta = \beta_0$ [23–28]. In this case the $f(r)$ function in Equation (1.28) is given by $f(r) = r^{2\beta_0}$, and by using this on Equation (1.26) it is possible to obtain the radial component of the velocity dispersion as

$$\sigma_{r,0}^2(r) = \left[\frac{GM_E}{R_E} \right] \frac{2}{\sqrt{\pi}\lambda(\alpha)(\xi - 2\beta_0)} \left(\frac{r}{R_E} \right)^{2-\alpha}. \quad (2.8)$$

where the sub-index 0 indicate that it was obtained using constant β , $\xi \equiv \alpha + \delta - 2$, R_E is the physical Einstein radius, and as M_E is the same mass as in Equation (1.10), the term in square bracket can be replaced using the lens' equation.

2.1.2 Osipkov-Merritt Model

The first radial model for β that we will introduce was presented independently by Osipkov [36] and Merritt [37]. Although it was proposed in the 1980's, it is still broadly used to solve problems in galactic dynamics [52, 57]. The Osipkov-Merritt (OM) model has its parameters fixed in the values $\beta_0 = 0$, $n = 2$ and $\beta_\infty = 1$, as result the OM anisotropy profile is given by

$$\beta_{\text{OM}}(r, r_a) = \frac{r^2}{r^2 + r_a^2}. \quad (2.9)$$

For this model, the $f(r)$ function in Equation (1.28) is $f(r) = r^2 + r_a^2$, and by using this on Equation (1.26) it is possible to obtain the radial component of the velocity dispersion as

$$\sigma_{r,\text{OM}}^2(r) = \left[\frac{GM_E}{R_E} \right] \frac{2}{\sqrt{\pi}\lambda(\alpha)\xi(\xi - 2)} \left(\frac{r}{R_E} \right)^{2-\alpha} \left[\xi - \frac{2r_a^2}{r^2 + r_a^2} \right]. \quad (2.10)$$

This expression is valid when $\delta + \alpha > 4$, if this condition is not satisfied, it leads to a divergence in Equation (1.26).

2.1.3 Mamon & Lokas Model

Next, we will solve the Jeans Equation for the Mamon & Lokas (ML) model presented in [35], for which $\beta_0 = 0$, $n = 1$ and $\beta_\infty = 1/2$, and the anisotropy profile is given by

$$\beta_{\text{ML}}(r) = \frac{1}{2} \frac{r}{r + r_a}. \quad (2.11)$$

In this case the $f(r)$ function in Equation (1.28) is given by $f(r) = r + r_a$, and the solution of the Jeans Equation is

$$\sigma_{r,\text{ML}}^2(r) = \left[\frac{GM_E}{R_E} \right] \frac{2}{\sqrt{\pi}\lambda(\alpha)\xi(\xi-1)} \left(\frac{r}{R_E} \right)^{2-\alpha} \left[\xi - \frac{r_a}{(r+r_a)} \right]. \quad (2.12)$$

For this model, the constraint on the slopes of the mass density and the brightness profile is $\delta + \alpha > 3$.

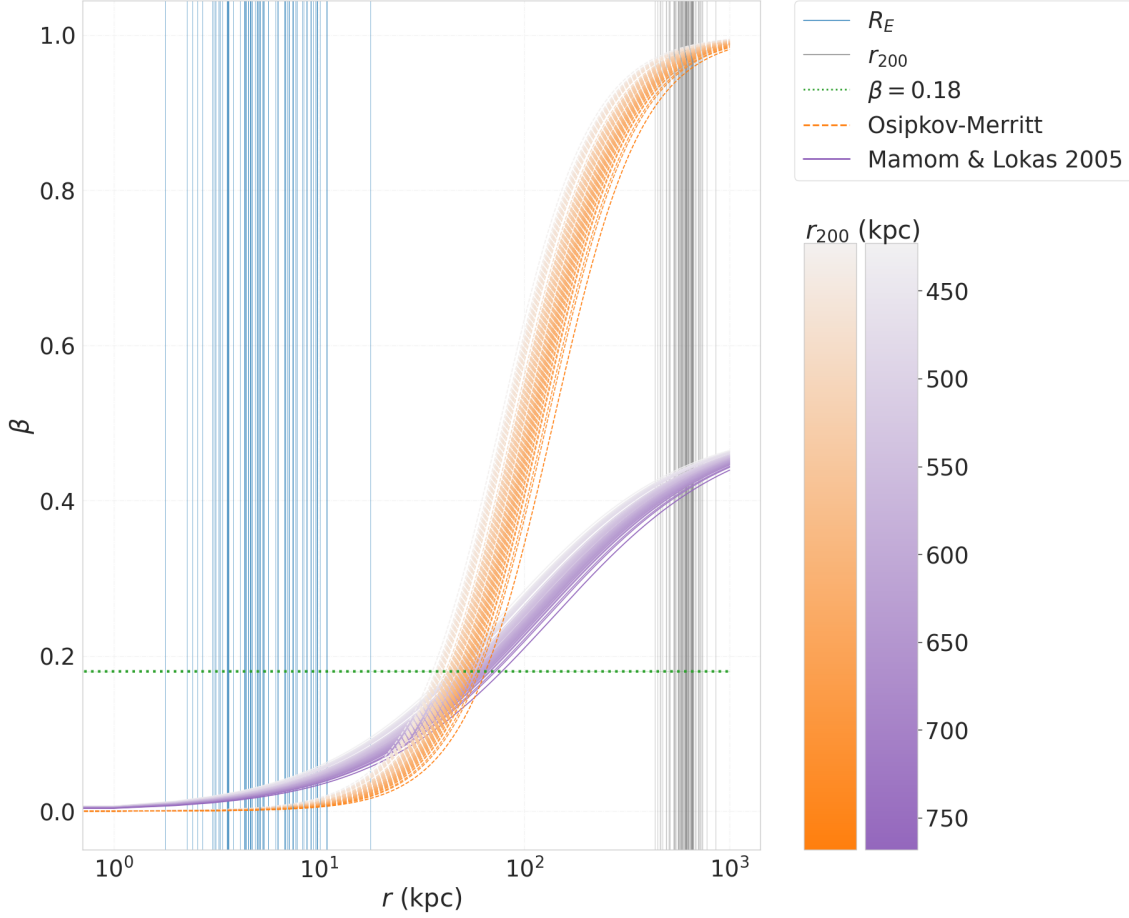


Figure 2.1: The radial behaviour of β profiles. As will be described in details on the texts, the orange dashed curves represent the Osipkov-Merritt Model, the purple solid lines represent the Mamon & Lokas model, and the dotted green line represents the constant anisotropy value used in [25]. On the left, the blue vertical lines denote the values of R_E for each system used in this analysis, and on the right, the black vertical lines denote their r_{200} values.

The behaviours of the aforementioned anisotropy profiles are depicted in Figure 2.1. The Osipkov-Merritt Model given by Equation (2.9) is represented by the orange dashed lines, while the Mamon & Lokas model given by Equation (2.11) is shown by the purple solid lines. The value of a suggested by [35], $a = 0.18$, was used in the calculations. Each line corresponds to a specific strong lensing system from the data set used in this work, which will be described in

Section 3.1 and presented in Table 3.1. The shade of orange or purple indicates the value of r_{200} for each system, obtained using Equation (2.4). The dotted green line represents the constant anisotropy value used in [25], $\beta = 0.18$. On the left, the blue vertical lines denote the values of R_E for each system, and on the right, the black vertical lines denote the corresponding r_{200} values.

From this figure, we can observe the asymptotic behaviour of the β profiles as r increases, determined by the parameter β_∞ which is fixed at 1 for the OM model and 0.5 for the ML model. Additionally, it is worth noting that the Einstein radius R_E corresponds to the radius at which the arcs in strong lensing (SL) systems appear. For the systems used for this study, the luminous radius of the lens galaxy is considerably smaller than R_E . The velocity dispersion is measured within the luminous radius, and consequently in a region where β is significantly small. Notably, r_{200} is significantly larger than both R_E and the luminous radius, as it accounts for all the matter in the galaxy, including baryonic and dark matter components.

2.1.4 Generalised Tired Model

Finally, we will examine a generalised version of Equation (2.11), given by

$$\beta_{GT} = \beta_0 + \beta_1 \frac{r}{r + r_a}. \quad (2.13)$$

This model is commonly known as Generalised Tired (GT) [38, 39], because it is a generalisation of the Tired model, presented in [38], where $\beta_0 = 0$. In the GT model, the function $f(r)$ is given by $f(r) = r^{2\beta_0}(r + r_a)^{2\beta_1}$. However, finding analytical solutions to Equation (1.26) using simple functions remains generally impossible for this model. Nevertheless, a solution can be obtained when β_1 is a half-integer, such as $1/2$ or 1 . To facilitate comparison with the ML model, we set β_1 to $1/2$. As a result, we obtain the following expression for the radial component of the stellar velocity dispersion

$$\sigma_{r,GT}^2(r) = \left[\frac{GM_E}{R_E} \right] \frac{2}{\sqrt{\pi}\lambda(\alpha)(\xi_1 - 3)(\xi_1 - 2)} \left(\frac{r}{R_E} \right)^{2-\alpha} \left[\xi_1 - 2 - \frac{r_a}{r + r_a} \right], \quad (2.14)$$

where $\xi_1 = \delta + \alpha - 2\beta_0$, and the condition $\delta + \alpha - 2\beta_0 > 3$ is satisfied.

2.2 Line-of-sight velocity dispersion and the observational conditions

In the previous section, we derived the radial component of the velocity dispersion of the stars in the lens galaxy. Nonetheless, it is not possible to measure the three-dimensional

components of the velocity dispersion. In order to compare the aforementioned models with observational data it is necessary to project σ_r onto the plane of the sky. Subsequently, it is required compute the mean value across the surface radius, taking into account both the surface brightness and a function that incorporates the observational conditions. In this section, we will demonstrate the process of performing these steps.

The velocity dispersion projected in the plane of the sky is known as the line-of-sight (LOS) velocity dispersion, σ_{LOS} . It is obtained by integrating σ_r^2 and the brightness profile ($\nu(r)$) along the line of sight. To calculate σ_{LOS} , we will use $\nu(r)$ defined in Equation (2.7), and adopt the approach introduced in [58]. This approach involves solving the following equation

$$\sigma_{LOS}^2(R) = \frac{2}{I(R)} \int_0^\infty \nu(r) \sigma_r^2 \left(1 - \frac{R^2}{r^2} \beta\right) dZ. \quad (2.15)$$

Here, $I(R)$ represents the projection of the brightness profile along the line of sight

$$I(R) = \int_{-\infty}^\infty \nu(r) dZ = \frac{\nu_0}{r_0^{-\delta}} \sqrt{\pi} \lambda(\delta) R^{1-\delta}. \quad (2.16)$$

For the first model introduced in the previous section it is possible to calculate the LOS velocity dispersion analytically. Specifically, when considering a constant anisotropy parameter β , we can use Equation (2.8) in Equation (2.15) to obtain

$$\sigma_{LOS,0}^2 = \left[\frac{GM_E}{R_E} \right] \frac{2[\lambda(\xi) - \beta_0 \lambda(\xi + 2)]}{\sqrt{\pi} \lambda(\delta) \lambda(\alpha) (\xi - 2\beta_0)} \left(\frac{R}{R_E} \right)^{2-\alpha}. \quad (2.17)$$

Nevertheless, for the subsequent models, namely OM, ML and GT, it is no longer possible to solve Equation (2.15) analytically. In order to overcome this challenge, we developed a numerical code to solve it. Details of this code will be discussed in Appendix A.

The next step to compare the models with observational data is to compute the mean of the squared velocity dispersion, $\langle \sigma_{LOS}^2 \rangle$. However, before proceeding, it is necessary to define a weighting function, $\omega(R)$. The data that will be used in this analysis have velocity dispersion measured by the *Sloan Digital Sky Survey* (SDSS) spectrograph, which has circular fibres with a radius of $1.5''$. Given that, in the case where the the fibre aperture θ_{ap} and the atmospheric seeing σ_{atm} satisfy the condition $\theta_{ap}/\sigma_{atm} < 1.5$, the function $\omega(R)$ can be treated as a Gaussian convolution of θ_{ap} and σ_{atm} , and approximated by [24]

$$\omega(R) \approx e^{-R^2/2D_L^2 \tilde{\sigma}_{atm}^2}, \quad (2.18)$$

where $\tilde{\sigma}_{atm}^2 \approx \sigma_{atm}^2 (1 + \chi^2/4 + \chi^4/40)$ and $\chi = \theta_{ap}/\sigma_{atm}$.

Following that, the mean velocity dispersion can be obtained by solving

$$\langle \sigma_{LOS}^2 \rangle = \frac{1}{N} \int_0^\infty \omega(R) I(R) \sigma_{LOS}^2(R) R dR, \quad (2.19)$$

where N is the normalisation factor given by

$$N = \int_0^\infty \omega(R) I(R) R dR = \frac{1}{2} \sqrt{\pi} \lambda(\delta) \Gamma\left(\frac{3-\delta}{2}\right) \left(\frac{2\tilde{\sigma}_{atm}^2}{\theta_E^2}\right)^{(3-\delta)/2} R_E^{(3-\delta)}. \quad (2.20)$$

Once again, it is possible to solve Equation (2.19) analytically for the model in which β is constant. By using Equation (2.17) we obtain

$$\langle \sigma_{LOS,0}^2 \rangle = \left[\frac{GM_E}{R_E} \right] \frac{2[\lambda(\xi) - \beta_0 \lambda(\xi + 2)]}{\sqrt{\pi} \lambda(\delta) \lambda(\alpha) (\xi - 2\beta_0)} \left(\frac{2\tilde{\sigma}_{atm}^2}{\theta_E^2} \right)^{(2-\alpha)/2} \frac{\Gamma\left(\frac{3-\xi}{2}\right)}{\Gamma\left(\frac{3-\delta}{2}\right)}. \quad (2.21)$$

As for the radial models of β , the integral in (2.19) will be solved numerically with the code described in Appendix A.

Finally, the square root of $\langle \sigma_{LOS}^2 \rangle$ mimics the observed value for the velocity dispersion. Our intention is to incorporate the effects that contribute to the observed quantity in order to directly compare the values obtained from the spectra. This defines the theoretical quantity $\bar{\sigma}_*$ from the modelling that should be directly compared to the velocity dispersion measured from the spectra

$$\bar{\sigma}_*(\mathbf{X}, \theta_E, z_L, z_S, \theta_{ap}, \sigma_{atm}) = \sqrt{\langle \sigma_{LOS}^2 \rangle}, \quad (2.22)$$

where $\theta_E, z_L, z_S, \theta_{ap}$ and σ_{atm} are the parameters obtained from observational data, and \mathbf{X} is the model parameters given by

$$\mathbf{X} = (\alpha, \delta, \beta_0, a; \gamma_{PPN}), \quad (2.23)$$

where α, δ, β_0 , and a are parameters associated with the ETGs' dynamics, and γ_{PPN} is the post-Newtonian parameter to be determined in this study. In the next section we will describe the application of $\bar{\sigma}_*(\mathbf{X}, \theta_E, z_L, z_S, \theta_{ap}, \sigma_{atm})$ in the statistical analysis.

2.3 Statistical Treatment

In the previous sections, we obtained the model $\bar{\sigma}_*(\mathbf{X}, \theta_E, z_L, z_S, \theta_{ap}, \sigma_{atm})$ for the velocity dispersion of an early-type galaxy. Now, we will describe how we use this model to fit the observed data. The data set employed consists of spectra obtained from the SDSS. Consequently, we will refer to the measured velocity dispersion as σ_{SDSS} .

In order to compare the modelled velocity dispersion with the measured values, we consider a Gaussian distribution for σ_{SDSS} . As a result, we can express the likelihood for each strong

lens system as [59]

$$\mathcal{L}_i(\sigma_{SDSS,i}|\bar{\sigma}_*) = \frac{1}{\sqrt{2\pi\varepsilon_{SDSS,i}^2}} \exp\left[-\frac{(\bar{\sigma}_* - \sigma_{SDSS,i})^2}{2\varepsilon_{SDSS,i}^2}\right], \quad (2.24)$$

where $\varepsilon_{SDSS,i}$ is the uncertainty in σ_{SDSS} . The likelihood for the whole sample is obtained by multiplying the likelihood of each individual system

$$\mathcal{L}(\{\sigma_{SDSS}\}|\bar{\sigma}_*) = \prod_{i=1}^N \mathcal{L}_i(\sigma_{SDSS,i}|\bar{\sigma}_*), \quad (2.25)$$

where N is the sample size. Equation (2.25) can result in very large values, which can be computationally demanding. For this reason, it is often more convenient to work with the logarithm of the likelihood, given by

$$\log(\mathcal{L}(\{\sigma_{SDSS}\}|\bar{\sigma}_*)) = \sum_{i=1}^N \log(\mathcal{L}_i(\sigma_{SDSS,i}|\bar{\sigma}_*)). \quad (2.26)$$

This can speed up the calculation and allow us to compute cases which otherwise would require special packages. Additionally, the logarithmic operation maintains the position of the maximum of the function.

One common approach to find the parameters \mathbf{X} that best fit the data is Maximum Likelihood Estimation (MLE), which involves maximising Equation (2.25), as for example through differentiation. However, as the complexity of the models increases, it becomes analytically intractable and we also faced computational challenges to solve it. To address this, we adopt a Bayesian approach. To begin, we define the posterior probability density function, $P(\mathbf{X}|\sigma_{SDSS})$, as

$$P(\mathbf{X}|\{\sigma_{SDSS}\}_i) \propto \mathcal{L}(\{\sigma_{SDSS}\}|\bar{\sigma}_*) \prod_i P(X_i), \quad (2.27)$$

where $P(X_i)$ represents the prior for each parameter of the model. To simplify the calculations, we can work with the logarithm of the posterior

$$\log(P(\mathbf{X}|\{\sigma_{SDSS}\}_i)) \propto \log(\mathcal{L}(\{\sigma_{SDSS}\}|\bar{\sigma}_*)) + \sum_i \log(P(X_i)). \quad (2.28)$$

The function of the priors is to incorporate prior knowledge about a parameter. For instance, in the case of ETGs the matter density slope α is approximated 2.0, that is the value of the SIS. This result has been supported by various studies that have successfully fitted the data [24, 25, 53], as well as N-body simulations [33, 49–51]. In this work we follow [25] and consider a Gaussian prior for α , $P(\alpha)$, centred in $\mu_\alpha = 2.0$ with a dispersion of $\sigma_\alpha = 0.08$. Additionally,

for the slope of the brightness profile, δ , we follow [24], which also employs a Gaussian prior for δ , $P(\delta)$, with mean $\mu_\delta = 2.4$ and dispersion $\sigma_\delta = 0.11$. Priors used for the parameters that characterise the anisotropy profile in the velocity dispersion, β_0 and a , will be discussed case-by-case in the next chapter. Finally, the post-Newtonian parameter γ_{PPN} is our parameter of interest, therefore, we consider its prior $P(\gamma_{PPN})$ to be flat and unbounded, and by doing this we do not insert any bias in its measurement.

To explore the parameter space, we employed Markov Chain Monte Carlo (MCMC) simulation [60]. This method generates Markov Chains (random walkers) by sampling from the probability distribution described in Equation (2.28). Consequently, a posterior distribution is obtained, which can then be used in a Gaussian kernel density estimator (KDE) [61] to derive the probability density functions (PDF) for each parameter. Subsequently, we can maximise the PDF for each parameter.

After obtaining the parameters that maximise the posterior, it is possible to calculate the χ^2 value for each model using [62]

$$\chi^2 = A - 2 \ln(\mathcal{L}(\mathbf{X}_{\max})) = \sum_{i=1}^N \frac{(\overline{\sigma}_*(\mathbf{X}_{\max}) - \sigma_{\text{SDSS},i})^2}{\varepsilon_{\text{SDSS},i}^2}. \quad (2.29)$$

Here, $\mathcal{L}(\mathbf{X}_{\max})$ represents the likelihood calculated using Equation (2.25) at the point \mathbf{X}_{\max} that maximises the posterior. The term A is the normalisation constant, $\overline{\sigma}_*(\mathbf{X}_{\max})$ is the model for the velocity dispersion discussed in Section 2.1 and calculated with the parameters that maximize the likelihood. Additionally, we calculate the reduced χ^2 as follows

$$\chi_{\text{red}}^2 = \frac{\chi^2}{N - k}, \quad (2.30)$$

where k is the number of parameters for which flat priors were used in the determination of the posterior probability. Furthermore, we compute the Bayesian Information Criterion (BIC) [63, 64] given by

$$\text{BIC} = k \ln(N) + \chi^2 \quad (2.31)$$

We selected the model employed by [25] as the null hypothesis and computed ΔBIC for each case. These metrics provide a means to compare the models with each other, aiding in the evaluation process. In the next chapter, we will present the main results obtained from this analysis.

Chapter 3

Results and Discussion

In this chapter we will present the results obtained by employing the methodology described in the previous chapter. In Section 3.1 we will discuss the data set used in these analyses. Following that, in Section 3.2 we will display the results of the Markov Chain Monte Carlo simulation used to explore the parameter space of the likelihood given in Equation (2.27). Finally, in Section 3.3 we will compare the results of the preceding section and present the best fits obtained for the post-Newtonian parameter.

3.1 Data set

Einstein Ring systems are relatively rare and difficult to detect, as an alignment of a few arc-seconds between the source and the line-of-sight of the lens is required [65]. Nevertheless, the emergence of the large-area surveys has significantly advanced the search for galaxy-galaxy strong lenses [65–68]. Oliveira et al. (in preparation) will publish a database with 31569 SL candidates, out of which 3601 system have measurements of z_S and z_L , and 409 have values of θ_E derived from Strong Lensing. After several quality cuts, they ended up with a sample containing about 206 systems that was used to constrain γ_{PPN} .

In a recent analyses, [27] used 120 strong lens systems to measure the post-Newtonian parameter. Notwithstanding the fact that the increase in sample size improves significantly the quality of the statistical analyses, it also introduces certain systematical challenges. For instance, the function in Equation (2.18) is specific for circular slits, while the sample includes data from rectangular slits, such that the modelling has to be adapted accordingly. In this work, we will apply the methodology presented in the previous Chapter to the same data set used by [25]. This approach enables a direct comparison of the effects of employing radial models for β , while keeping all other aspects of the modelling identical.

All the strong lensing systems used in this study were compiled by [69] and are listed in Table 3.1. The information presented in its columns is the name of each system, the redshift

of the lens (z_L), the redshift of the source (z_S), the Einstein radius (θ_E), the circular fiber radius (θ_{ap}), the atmospheric seeing (σ_{atm}) (all three in arc-seconds), the velocity dispersion measured from the spectra (σ_{SDSS}) in kilometres per second, and the name of the survey where the system where discovered. Each row corresponds to one of the 80 systems used in this work, including 13 systems from the *Baryon Oscillation Spectroscopic Survey* (BOSS) *Emission-Line Lens Survey* (BELLS) [70], 22 from the *Strong lensing Legacy Survey* (SL2S) [71, 72], 42 from the *Sloan Lens Advanced Camera for Surveys* (SLACS) [73, 74], and 3 systems from a SLACS' precursor, known as the *Lenses Structure and Dynamics Survey* (LSD) [75, 76].

Name	z_L	z_S	θ_E (")	θ_{ap} (")	σ_{atm} (")	σ_{SDSS} (km/s)	Survey
J0747+4448	0.437	0.897	0.61	1	1.8	281 ± 52	BELLS
J1637+1439	0.391	0.874	0.65	1	1.8	208 ± 30	BELLS
J2303+0037	0.458	0.936	1.02	1	1.8	274 ± 31	BELLS
J2125+0411	0.363	0.978	1.2	1	1.8	247 ± 17	BELLS
J0151+0049	0.517	1.364	0.68	1	1.8	219 ± 39	BELLS
J0830+5116	0.530	1.332	1.14	1	1.8	268 ± 36	BELLS
J0944-0147	0.539	1.179	0.72	1	1.8	204 ± 34	BELLS
J1545+2748	0.522	1.289	1.21	1	1.8	250 ± 37	BELLS
J1337+3620	0.564	1.182	1.39	1	1.8	225 ± 35	BELLS
J1542+1629	0.352	1.023	1.04	1	1.8	210 ± 16	BELLS
J1215+0047	0.642	1.297	1.37	1	1.8	262 ± 45	BELLS
J1601+2138	0.544	1.446	0.86	1	1.8	207 ± 36	BELLS
J1631+1854	0.408	1.086	1.63	1	1.8	272 ± 14	BELLS
HST14176+5226	0.810	3.399	1.41	1.25	0.75	224 ± 15	LSD
CFRS03.1077	0.938	2.941	1.24	1.25	0.8	251 ± 19	LSD
Q0047-2808	0.485	3.595	1.34	1.25	0.7	229 ± 15	LSD
J2203+0205	0.400	2.15	1.95	1	0.9	213 ± 21	SL2S
J1411+5651	0.322	1.42	0.93	1	1.3	214 ± 23	SL2S
J0855-0409	0.419	2.95	1.36	0.7	0.6	281 ± 22	SL2S
J0213-0743	0.717	3.48	2.39	1	0.6	293 ± 34	SL2S
J1406+5226	0.716	1.47	0.94	1	0.9	253 ± 19	SL2S
J0217-0513	0.646	1.847	1.27	1.5	0.6	239 ± 27	SL2S
J1405+5243	0.526	3.01	1.51	1	0.8	284 ± 21	SL2S
J0223-0534	0.499	1.44	1.22	1	0.6	288 ± 28	SL2S
J0226-0420	0.494	1.232	1.19	1	0.6	263 ± 24	SL2S

Continued on next page

Name	z_L	z_S	θ_E (")	θ_{ap} (")	σ_{atm} (")	σ_{SDSS} (km/s)	Survey
J1420+5630	0.483	3.12	1.4	1	0.8	228 ± 19	SL2S
J0214-0405	0.609	1.88	1.41	1	0.8	287 ± 47	SL2S
J2222+0012	0.436	1.36	1.44	1	0.9	221 ± 22	SL2S
J0225-0454	0.238	1.199	1.76	1	0.7	234 ± 21	SL2S
J0212-0555	0.750	2.74	1.27	0.9	0.7	273 ± 22	SL2S
J0849-0251	0.274	2.09	1.16	0.9	0.8	276 ± 35	SL2S
J0855-0147	0.365	3.39	1.03	0.7	0.6	222 ± 25	SL2S
J1420+5258	0.380	0.99	0.96	1	0.8	246 ± 23	SL2S
J0232-0408	0.352	2.34	1.04	1	0.7	281 ± 26	SL2S
J0219-0829	0.389	2.15	1.3	1	0.7	289 ± 23	SL2S
J2221+0115	0.325	2.35	1.4	1	1.2	222 ± 23	SL2S
J1359+5535	0.783	2.77	1.14	1	0.7	228 ± 29	SL2S
J0850-0347	0.337	3.25	0.93	0.7	0.6	290 ± 24	SL2S
J1636+4707	0.228	0.674	1.09	1.5	1.4	231 ± 15	SLACS
J1020+1122	0.282	0.553	1.2	1.5	1.4	282 ± 18	SLACS
J1630+4520	0.248	0.793	1.78	1.5	1.4	276 ± 16	SLACS
J1621+3931	0.245	0.602	1.29	1.5	1.4	236 ± 20	SLACS
J0822+2652	0.241	0.594	1.17	1.5	1.4	259 ± 15	SLACS
J1250+0523	0.232	0.795	1.13	1.5	1.4	252 ± 14	SLACS
J2300+0022	0.228	0.464	1.24	1.5	1.4	279 ± 17	SLACS
J1402+6321	0.205	0.481	1.35	1.5	1.4	267 ± 17	SLACS
J0109+1500	0.294	0.525	0.69	1.5	1.4	251 ± 19	SLACS
J1251-0208	0.224	0.784	0.84	1.5	1.4	233 ± 23	SLACS
J1142+1001	0.222	0.504	0.98	1.5	1.4	221 ± 22	SLACS
J0946+1006	0.222	0.608	1.38	1.5	1.4	263 ± 21	SLACS
J0808+4706	0.219	1.025	1.23	1.5	1.4	236 ± 11	SLACS
J1205+4910	0.215	0.481	1.22	1.5	1.4	281 ± 14	SLACS
J1627-0053	0.208	0.524	1.23	1.5	1.4	290 ± 14	SLACS
J0728+3835	0.206	0.688	1.25	1.5	1.4	214 ± 11	SLACS
J0037-0942	0.196	0.632	1.53	1.5	1.4	279 ± 10	SLACS
J1023+4230	0.191	0.696	1.41	1.5	1.4	242 ± 15	SLACS
J0029-0055	0.227	0.931	0.96	1.5	1.4	229 ± 18	SLACS
J1416+5136	0.299	0.811	1.37	1.5	1.4	240 ± 25	SLACS
J1531-0105	0.160	0.744	1.71	1.5	1.4	279 ± 14	SLACS

Continued on next page

Name	z_L	z_S	θ_E (")	θ_{ap} (")	σ_{atm} (")	σ_{SDSS} (km/s)	Survey
J1106+5228	0.096	0.407	1.23	1.5	1.4	262 ± 13	SLACS
J0903+4116	0.430	1.065	1.29	1.5	1.4	223 ± 27	SLACS
J1525+3327	0.358	0.717	1.31	1.5	1.4	264 ± 26	SLACS
J0157-0056	0.513	0.924	0.79	1.5	1.4	295 ± 47	SLACS
J2321-0939	0.082	0.532	1.6	1.5	1.4	249 ± 8	SLACS
J1436-0000	0.285	0.805	1.12	1.5	1.4	224 ± 17	SLACS
J1403+0006	0.189	0.473	0.83	1.5	1.4	213 ± 17	SLACS
J2341+0000	0.186	0.807	1.44	1.5	1.4	207 ± 13	SLACS
J1153+4612	0.180	0.875	1.05	1.5	1.4	226 ± 15	SLACS
J0936+0913	0.190	0.588	1.09	1.5	1.4	243 ± 12	SLACS
J1016+3859	0.168	0.439	1.09	1.5	1.4	247 ± 13	SLACS
J2303+1422	0.155	0.517	1.62	1.5	1.4	255 ± 16	SLACS
J1134+6027	0.153	0.474	1.1	1.5	1.4	239 ± 12	SLACS
J1218+0830	0.135	0.717	1.45	1.5	1.4	219 ± 11	SLACS
J1451-0239	0.125	0.52	1.04	1.5	1.4	223 ± 14	SLACS
J1213+6708	0.123	0.64	1.42	1.5	1.4	292 ± 15	SLACS
J0044+0113	0.120	0.196	0.79	1.5	1.4	266 ± 13	SLACS
J0841+3824	0.116	0.657	1.41	1.5	1.4	225 ± 11	SLACS
J1143-0144	0.106	0.402	1.68	1.5	1.4	269 ± 13	SLACS
J1204+0358	0.164	0.631	1.31	1.5	1.4	267 ± 17	SLACS
J0330-0020	0.351	1.071	1.1	1.5	1.4	212 ± 21	SLACS

Table 3.1: The compilation of the Data Set used in this analysis.

In Figure 3.1 we summarise two properties of the data set that we have given special attention to. Firstly, Figure 3.1(a) presents a histogram illustrating the distribution of the r_{200} for the 80 lenses in this sample, derived using Equation (2.4). It is possible to notice that this radius falls within the range of a few hundred kiloparsecs, which is consistent with the expected values for ETGs. This quantity is used to obtain the characteristic radius (r_a) for the β models discussed in Section 2.1. Secondly, Figure 3.1(b) displays the redshifts of the lenses. It is clear that all the lenses have redshift values below 1 ($z_l < 1$), allowing us to use the results of [33], which indicate that the slope of the density profile, α , remains nearly constant at approximately 2 for galaxies at these redshifts. In the next section we will present the results obtained for this data set after applied the methodology described in Chapter 2.

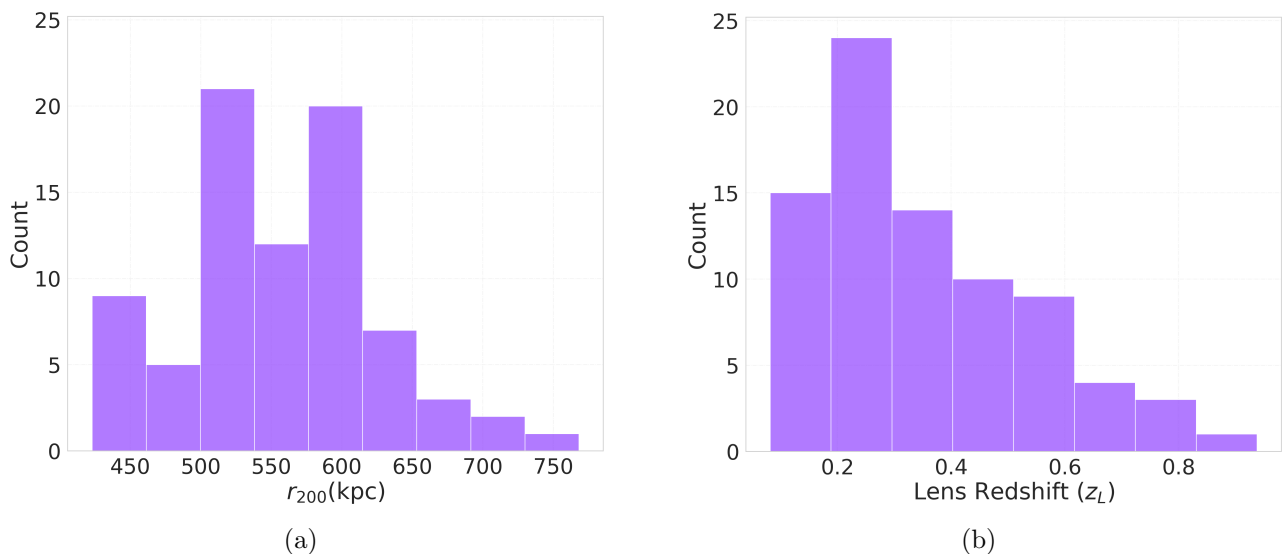


Figure 3.1: Some properties of the lenses in the data set: (a) the distribution of r_{200} of the lenses in this sample, derived from Equation (2.4) and (b) the distribution of the lens redshifts.

3.2 Results of the Markov Chain Monte Carlo Simulation

In this section, we present the results of the Monte Carlo Markov Chain (MCMC) simulation conducted to explore the parameter space of Equation (2.27), for different models characterising the anisotropy between the radial and tangential components of the velocity dispersion in the lens galaxy. The statistical treatment employed in the MCMC analysis is outlined in Section 2.3, and the analysis is applied to the data set described in the previous section.

3.2.1 Constant Anisotropy Parameter β_0

The model in which the anisotropy parameter is constant, $\beta = \beta_0$, is described in the Section 2.1.1. This model has four parameters, namely the mass density slope α , the brightness profile slope δ , the anisotropy parameter β_0 , and the post-Newtonian parameter $\gamma_{PPN,0}$. To begin, we investigated the impact of three different Gaussian priors for β_0 . Firstly, we replicated the findings of [25], who used a prior of $\beta_0 = 0.18 \pm 0.13$. Subsequently, we adopted a prior based on measurements conducted by [53], where strong lensing data was used to analyse the dynamics of ETGs and they obtained $\beta_0 = 0.45 \pm 0.25$. Furthermore, we incorporated the outcomes from the studies of [33] on galaxy dynamics, where they obtained $\beta_0 = 0.23 \pm 0.19$ using a simulated data set of ETGs. Additionally, we also considered the scenario of a flat prior, ranging between 0 and 1, for the anisotropy parameter.

The MCMC results for the three Gaussian priors are compiled in in Figure 3.2. This corner

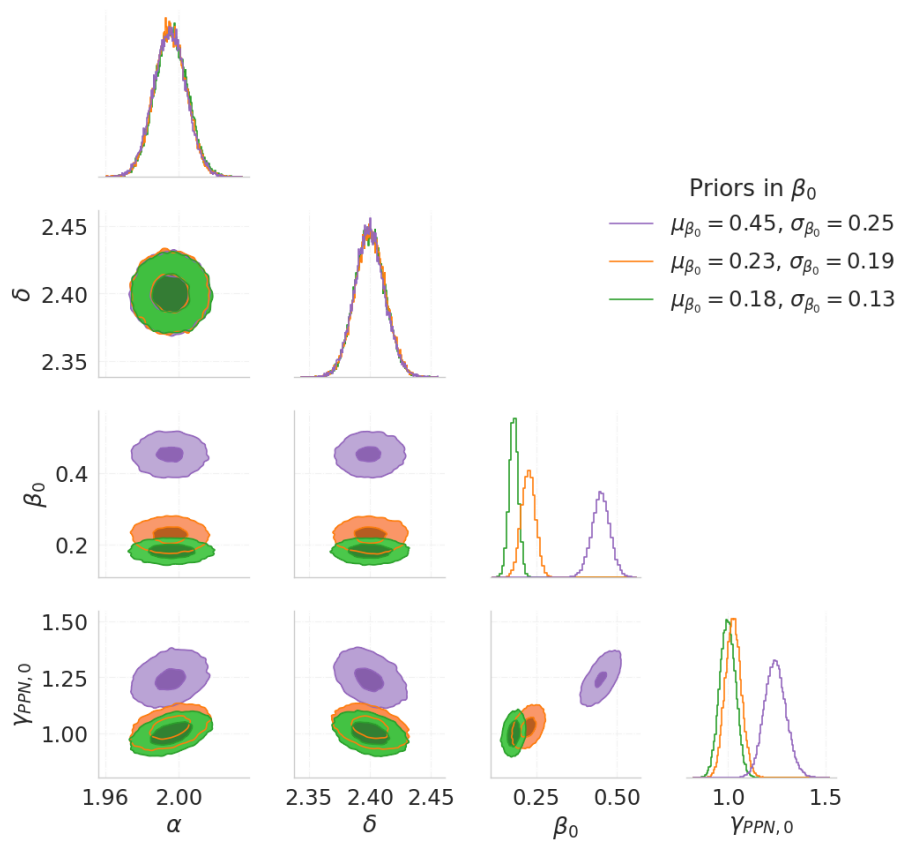


Figure 3.2: Result of the Markov Chain Monte Carlo for the model with β constant and with a Gaussian prior. The purple distributions are the result for the β_0 with Gaussian prior centred in $\mu_{\beta_0} = 0.45$, the orange distributions are for $\mu_{\beta_0} = 0.23$, and the green distributions are the results for $\mu_{\beta_0} = 0.18$. The shade of green, orange or purple in the bivariate distributions indicate the density of data points, and the contours correspond to the 50th and 95th percentiles.

plot provides an overview of the parameters phase space explored by the random walkers in the Markovian Chains. The lower sections of the plot illustrate the multivariate distribution of these parameters, allowing us to gain insights on the correlation between them. The diagonal displays the individual distribution for each parameter. The green distributions represent the reproduction of the results in reference [25], the orange ones corresponds to the results obtained when used the prior based on the study conducted by [33], and the purple distributions were obtained with the prior derived from the measurements of [53].

The first two parameters in the left of the Figure 3.2 are α and δ . As expected, their posterior distributions follow closely their prior described in section 2.3. Moreover, there is no apparent correlation between these parameters and any other. Moving to the third parameter, β_0 , it is possible to observe a significant correlation with $\gamma_{PPN,0}$. Lastly, the fourth parameter is the post-Newtonian parameter. Although this was the only parameter with a flat prior in this analysis, for this case, its posterior also presents a Gaussian profile. This is a confirmation that it is possible to use this methodology to constrain $\gamma_{PPN,0}$. A broader discussion on the posterior obtained for the post-Newtonian parameter will be presented in Section 3.3.

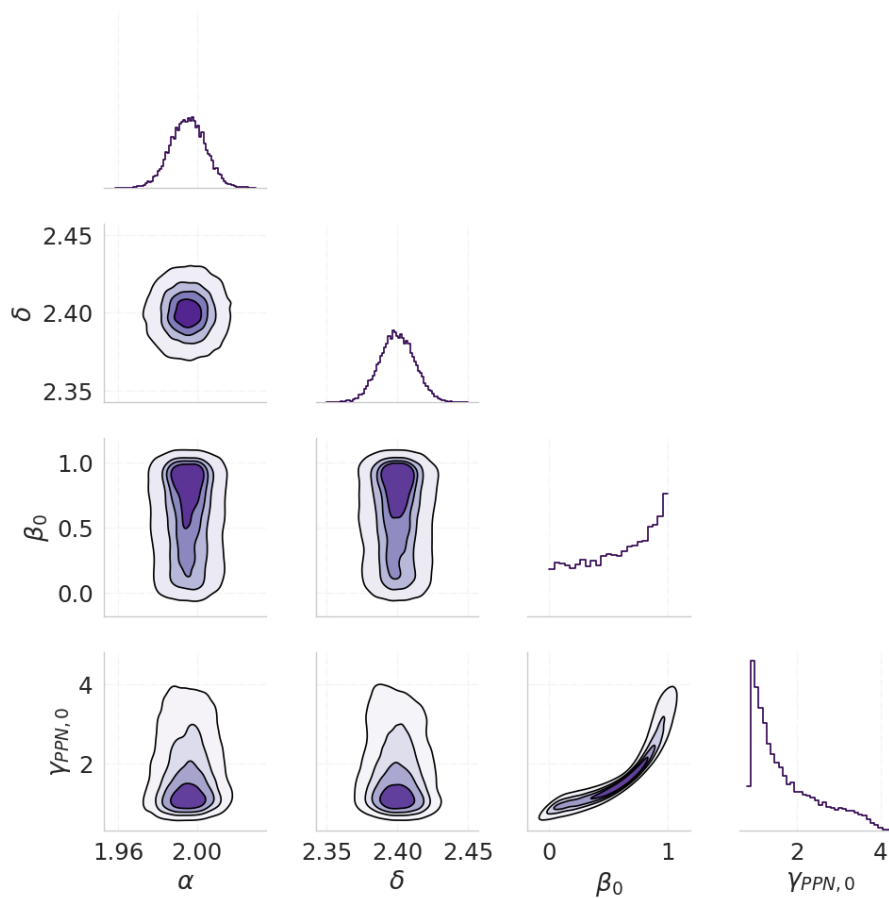


Figure 3.3: Corner plot with the result for the Markov Chain Monte Carlo, for the model with β constant and with a flat $P(\beta_0)$, varying between 0 and 1. The shades in the bivariate distributions indicate the density of data points.

The results of the MCMC simulation with a flat prior on β_0 , are summarised on Figure 3.3. Similar to the previous case, the two first parameters, α and δ show no apparent correlation between them and the other parameters, and also maintain their Gaussian posterior. For this case the correlation between β_0 and $\gamma_{PPN,0}$ is very strong. The posterior distribution of β_0 increases until it reaches one, that is the value by which this parameter is limited by the prior. This behaviour is explained by the fact that β_0 is limited by one. Regarding $\gamma_{PPN,0}$, its posterior distribution deviates from a Gaussian profile when the prior in β_0 is considered flat. This shows that when β is left unconstrained, this method is able to place only weak constraints on $\gamma_{PPN,0}$. Nevertheless, the distribution still tends to favour values close to one.

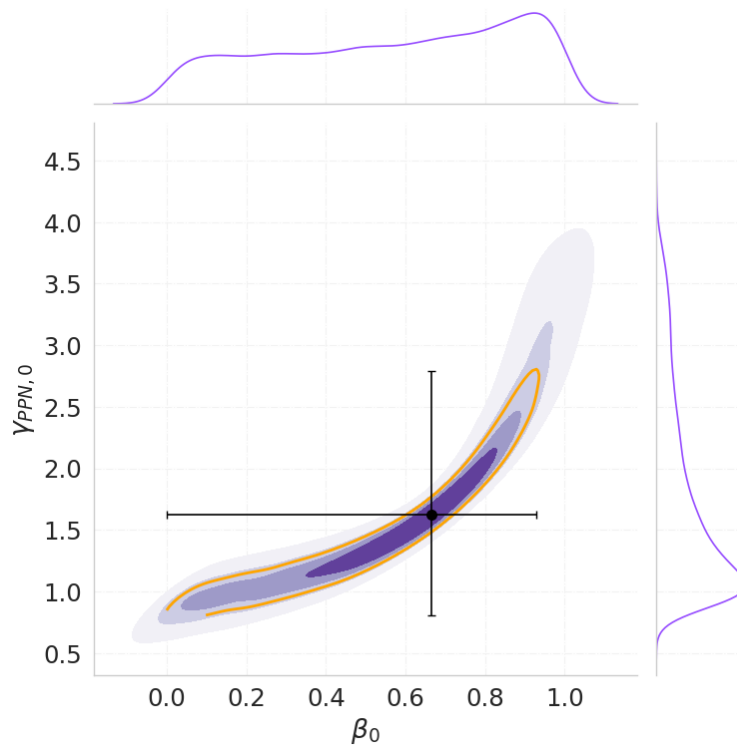


Figure 3.4: Bivariate distribution of the free parameters β_0 and $\gamma_{PPN,0}$, for the model with β constant and with a flat prior. The shades of purple distributions indicate the density of data points. The black point in the middle is the mode of the bivariate distribution function, obtained by maximising this function. The orange curve marks the 1σ interval, and the error bars are obtained by calculating the maximum distance between the mode and the 1σ interval.

It is possible to examine the relationship between $\gamma_{PPN,0}$ and β_0 more closely in Figure 3.4. These particular parameters are the only ones with a flat prior, which means they represent the free parameters of this model. Therefore, we can analyse their bivariate posterior and maximise it accordingly. The black point in the middle represents the maximum point of the bivariate distribution, corresponding to $\beta_0 = 0.67^{+0.26}_{-0.67}$ and $\gamma_{PPN,0} = 1.62^{+1.17}_{-0.82}$, the uncertainties are considered as the maximum distance between the point that maximises the bivariate distribution and the 1σ interval. Additionally, the 68.27% confidence interval is highlighted in orange.

3.2.2 Osipkov-Merritt Model

The Osipkov-Merritt (OM) model, defined in Equation (2.9), is discussed in Section 2.1.2. This model has four parameters, namely the mass density slope α , the brightness profile slope δ , the parameter a that sets the scale radius of the model ($r_a = r_{200}a$), and the post-Newtonian parameter $\gamma_{PPN,OM}$. As we did not have an accurate measurement of a and its uncertainties from the literature, we considered its prior to be flat, and let it vary between 0 and 10.

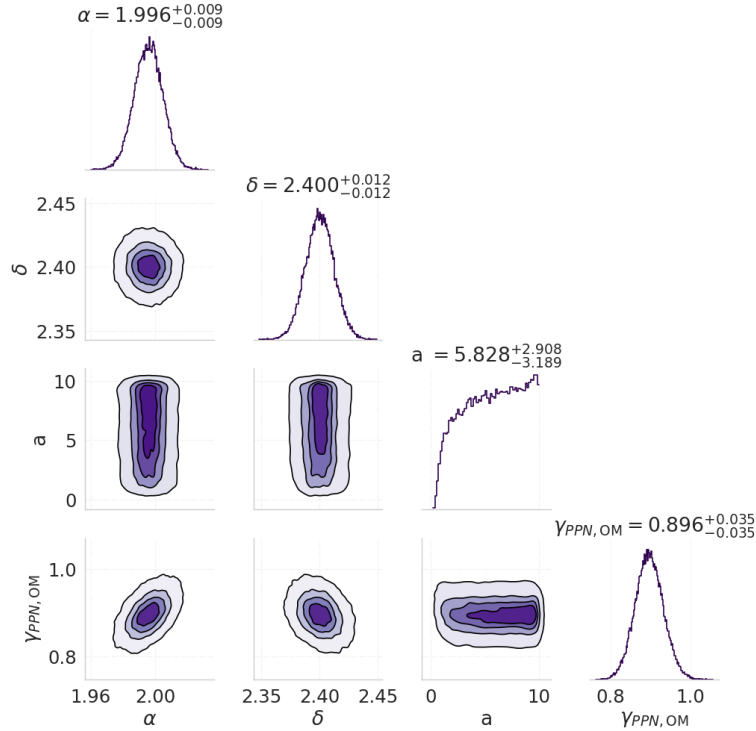


Figure 3.5: Corner plot with the result for the Markov Chain Monte Carlo the Osipkov-Merritt Model For radial β . The shades of purple and the contours in the bivariate distributions indicate the density of data points and also add a third dimension to the plot, indicating the increase in the density.

The MCMC result for this model is compiled in Figure 3.5. Each diagonal plot in the figures is labelled with the parameter median, which corresponds to the 50th percentile. Additionally, the distances from the median to the 84th and 16th percentiles are indicated, providing a measure of the parameter uncertainty. The posterior distribution of the first two parameters, α and δ , are essentially the same as their Gaussian priors discussed in Section 2.3. The third parameter, a , shows a nearly flat posterior, indicating that this parameter could not be effectively constrained using this methodology. Nevertheless, the data clearly favours values $a > 1.7$. In contrast, the fourth parameter, $\gamma_{PPN,OM}$, presents a Gaussian-like posterior distribution, which implies that this model allow us to successfully constraint this parameter. Furthermore, there is no evident correlation observed among any of the parameters in this particular model.

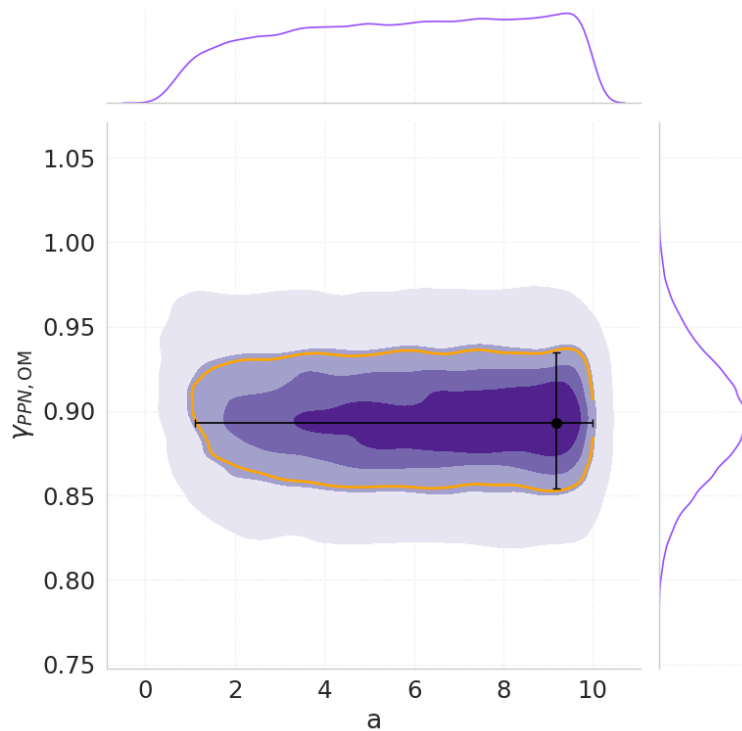


Figure 3.6: Bivariate distribution of the free parameters a and $\gamma_{PPN,OM}$, for the model with the Osipkov-Merritt profile for β . The shades of purple distributions indicate the density of data points. The black point in the middle is the mode of the bivariate distribution function, obtained by maximising this function. The orange curve marks the 1σ interval, and the error bars are obtained by calculating the maximum distance between the mode and the 1σ interval.

In this scenario, the free parameters are a and $\gamma_{PPN,OM}$, their bivariate distribution is shown in Figure 3.6. As mentioned before, it is clear from this plot, that the posterior PDF for a is almost flat. It goes to zero below 0 and 10, which are exactly the boundaries of our prior. Therefore, this data has very little constraint power for a . Perhaps, lower values of a , close to 0 are disfavoured. This could be further tested by modifying the range of the flat prior. We see a slight increase of the PDF for higher a . In brief the parameter a is largely constrained by the data perhaps excluding too low values of a which means that β is very low at r_{200} and, in particular at the optical radius, which is constrained by the optical data (see Figure 2.1). In this figure the orange contour outlines the 1σ interval, and the black dot represents the point of highest density, at $a = 9.19^{+0.81}_{-8.09}$ and $\gamma_{PPN,OM} = 0.89^{+0.04}_{-0.04}$, the uncertainties are considered as the maximum distance between the point that maximises the bivariate distribution and the 1σ interval. Again, whereas $\gamma_{PPN,OM}$ is well constrained by the data, the bounds on a largely reflect the choice of boundary of the flat prior. Our result is compatible with 1 only above 2.5σ .

3.2.3 Mamon & Lokas Model

The radial model proposed by Mamon & Lokas (ML) is defined in the Equation (2.11) and discussed in Section 2.1.3. This model has four parameters, namely the mass density slope α , the brightness profile slope δ , the parameter a that sets the scale radius of the model ($r_a = r_{200}a$), and the post-Newtonian parameter $\gamma_{PPN,ML}$. The prior for a was, again, considered flat and allowed to vary between 0 and 10. The MCMC result for this model is shown in Figure 3.7, and the interpretation of this figure is similar to the one described in the previous section.

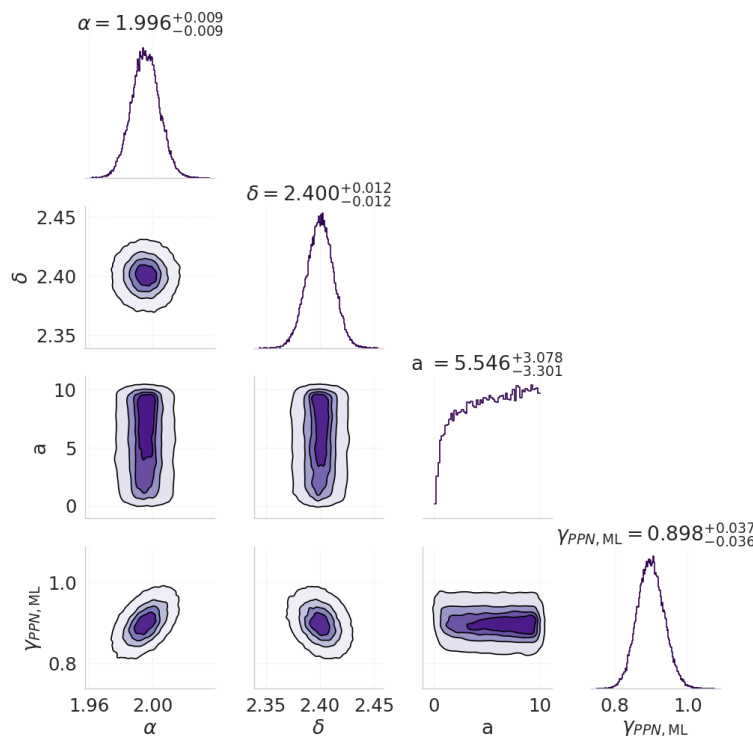


Figure 3.7: Corner plot with the result for the Markov Chain Monte Carlo the Mamon & Lokas Model for radial β . The shades of purple and the contours in the bivariate distributions indicate the density of data points and also add a third dimension to the plot, indicating the increase in the density.

As in the previous case, the posterior distributions of the initial two parameters, α and δ , correspond closely to their Gaussian priors as described in Section 2.3. The third parameter, a , exhibits an almost uniform posterior distribution, suggesting that this parameter cannot be effectively constrained using this approach. Nevertheless, the data clearly favours values $a > 1.5$. Conversely, the $\gamma_{PPN,ML}$ demonstrates a posterior distribution that resembles a Gaussian curve, indicating successful constrain of this parameter. Moreover, no apparent correlation is observed among any of the parameters in this specific model.

The behaviour of the free parameters in this particular case, namely a and $\gamma_{PPN,ML}$, is illustrated in Figure 3.8. Within the plot, the 68.27% confidence interval is visually emphasised

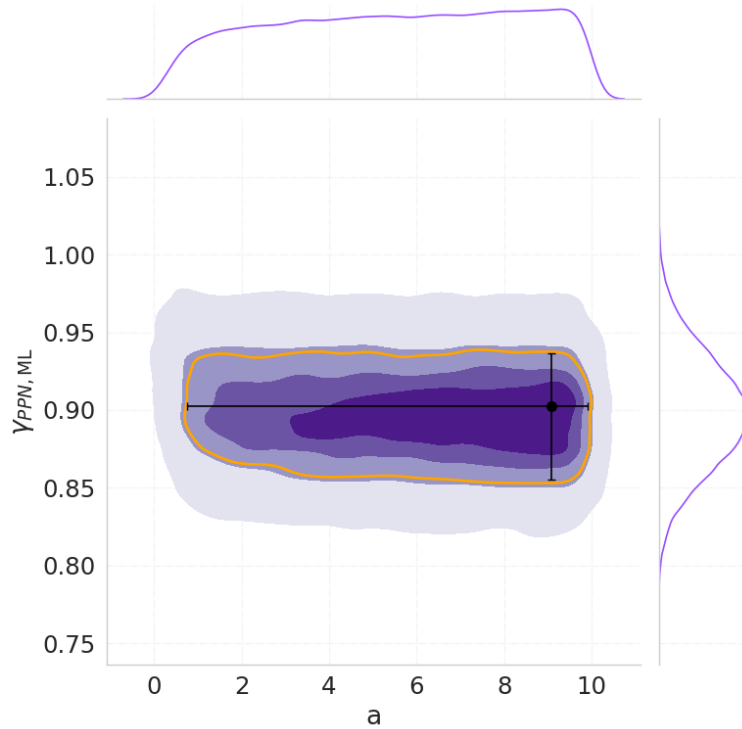


Figure 3.8: Bivariate distribution of the free parameters a and $\gamma_{PPN,ML}$, for the model with the Mamon & Lokas profile for β . The black point in the middle is the mode of the bivariate distribution function, obtained by maximising this function. The orange curve marks the 68.27% confidence interval, and the error bars are obtained by calculating the maximum distance between the mode and the 68.27% confidence interval.

using an orange contour. At the peak of the distribution, we find a black dot representing the optimal values of $a = 9.07_{-8.33}^{+0.83}$ and $\gamma_{PPN,ML} = 0.90_{-0.05}^{+0.03}$. The uncertainties are defined as the maximum separation between the point that maximises the bivariate distribution and the 1σ interval. In this case, again, the derived bounds on a reflect the choice of the prior, whereas $\gamma_{PPN,ML}$ can be constrained with a relatively good precision. The result are consistent with $\gamma_{PPN} = 1$ only at the 2.5σ level.

3.2.4 Generalised Tired Model

The last model tested for the anisotropy profile of the lens galaxy is the generalisation of the Tired model, discussed in Section 2.1.4. We solved Equation (2.13) for the case where $\beta_1 = 0.5$, and it resulted in the velocity dispersion model (Equation (2.22)) that uses the five parameters from Equation (2.23). As before, these parameters are the mass density slope α , the brightness profile slope δ , the constant anisotropy value for low radii β_0 , the parameter that scales the control radius in the β model a , and the post-Newtonian parameter $\gamma_{PPN,GT}$. The priors for both β_0 and a were considered flat for this model, therefore they are treated as free parameters. We allowed β_0 to vary between 0 and 1, and a to vary between 0 and 10. The MCMC results

for this model are summarised in Figure 3.9, and the interpretation for this figure is analogous to the previous cases.

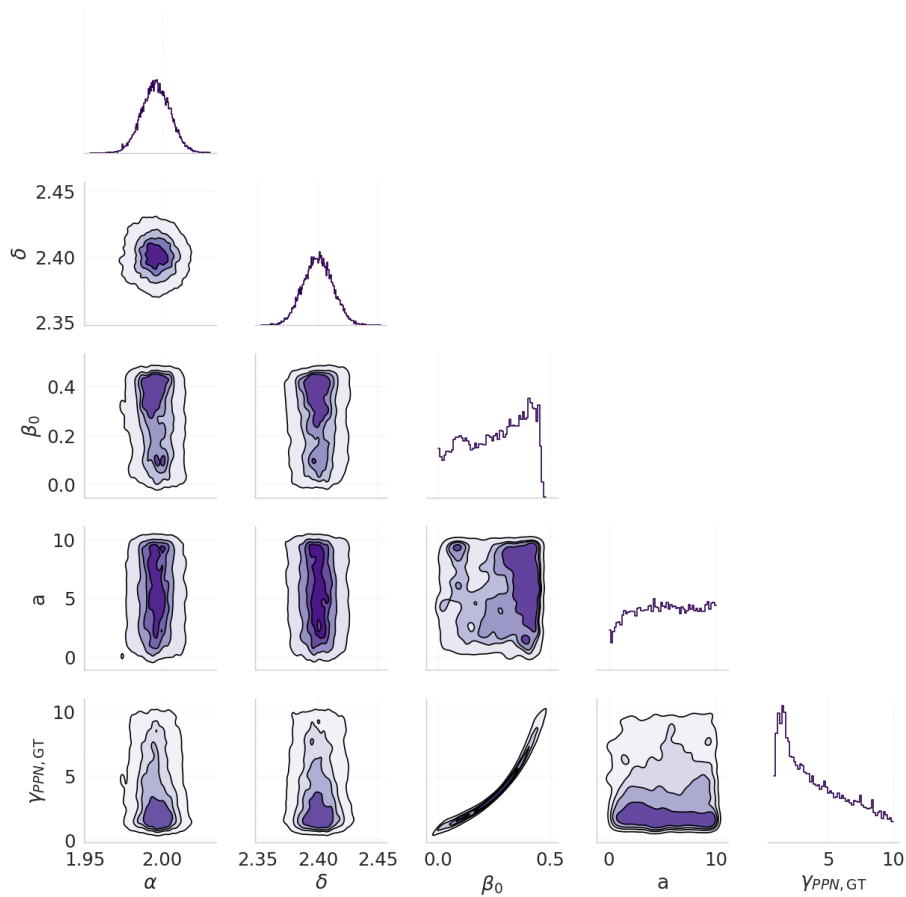


Figure 3.9: Corner plot with the result for the Markov Chain Monte Carlo the Generalised Tired Model for radial β , with $\beta_1 = 0.5$. The shades of purple and the contours in the bivariate distributions indicate the density of data points and also add a third dimension to the plot, indicating the increase in the density.

Moreover, the posterior distribution of the third parameter β_0 presents a moderate ascendant profile, similar to what was observed in Figure 3.3, for the case when a flat prior in β_0 was also used, but with the assumption of constant anisotropy along the galaxy radius. In this case, however, β_0 is being limited by the data to 0.5 instead of 1, despite the fact that it was allowed to vary until 1 during this simulation. This behaviour can be explained by referring back to Equation (2.13), which shows that as r approaches infinity, $\beta(r)$ tends towards $\beta_0 + \beta_1 = \beta_\infty$. Given that the anisotropy parameter is limited to values less than or equal to one (Equation 1.20), it follows that $\beta_0 + \beta_1 \leq 1$. Therefore, if β_1 is fixed at 0.5, then β_0 must be ≤ 0.5 . Finally, β_0 continues to present a positive correlation with the post-Newtonian parameter.

Furthermore, the third parameter, a , displays a nearly flat posterior, that align with its prior. That is equivalent to what happens in Figures 3.5 and 3.7, confirming that the scale

parameter of the reference radius in the radial model for β can not be constrained using this methodology. On the other hand, as in the previous models of $\beta(r)$ low values of a (< 1.3) seem to be disfavoured by the data.

Lastly, the posterior of the free parameter, $\gamma_{PPN,GT}$, in Figure 3.9 does not present a Gaussian profile. As the case $\beta = \beta_0$ with a flat prior on β_0 (Figure 3.3) it is no longer possible to effectively constrain the post-Newtonian parameter. Yet, the distribution still tends to favour values next to one.

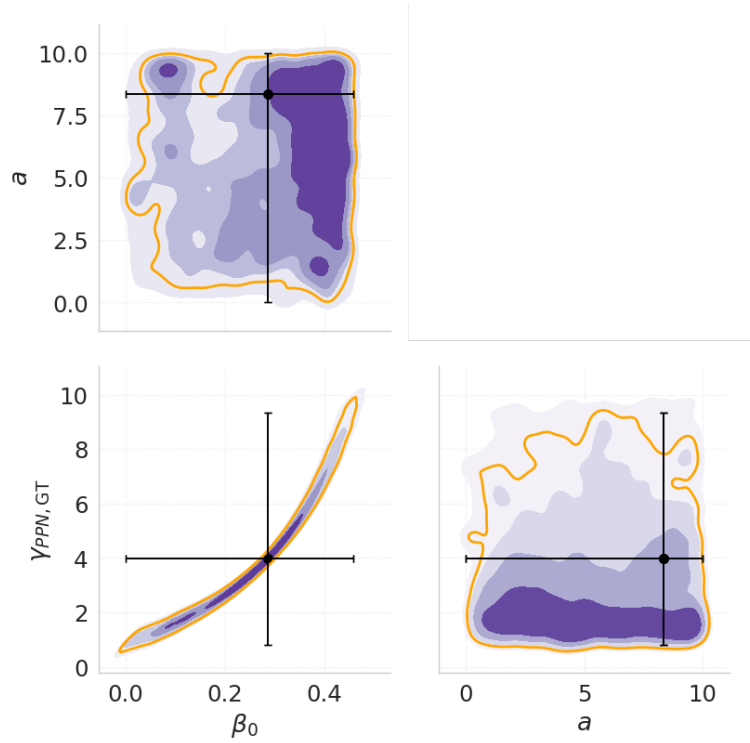


Figure 3.10: Multivariate distribution of the free parameters β_0 , a and $\gamma_{PPN,GT}$, for the model with the Generalised Tired profile for radial β , with $\beta_1 = 0.5$. The density of data points is represented by the varying shades of purple in the distributions. The central black point corresponds to the mode of the bivariate distribution function, which is obtained by maximising this function. The orange curve denotes the 1σ interval, and the error bars are determined by measuring the maximum distance between the mode and the 1σ interval.

This particular model consists of three free parameters: β_0 , a , and $\gamma_{PPN,GT}$. The multivariate distribution of these parameters can be visualised in Figure 3.10. One notable observation is the significant statistical fluctuation present in the density distribution of these model parameters. This can be attributed to the fact that this model has the largest number of free parameters, making it computationally demanding. Within the plot, the orange curve indicates the 1σ interval for each parameter. The black dot represents the point of highest density, at $\beta_0 = 0.29^{+0.17}_{-0.29}$, $a = 8.343^{+1.66}_{-8.34}$, and $\gamma_{PPN,0} = 3.97^{+5.38}_{-3.15}$. The uncertainties are quantified as the maximum difference between the point that maximises the bivariate distribution and the 1σ

interval. Even more strongly than in the previous cases, the bound on a is essentially determined by the boundaries of the flat prior. The lower bound on β_0 is also determined by the choice of the prior, whereas it is naturally limited by the data to $\beta_0 \simeq 0.5$.

3.3 Posterior Probability Density Function and Model Fitting

In the previous section, we discussed 3 classes of models for β . The first has $\beta = \beta_0 = \text{const.}$ and we considered 3 sets of Gaussian priors from different origins, as well as a case with a flat prior (spanning $\beta_0 = 0$ to 1). The second class refers to models where β has a radial dependence, starts with $\beta = 0$ and goes to a fixed asymptotic value at high distances. They have a characteristic radius given by $r_a = ar_{200}$, these are the OM model and the ML model. Finally, the third class is a generalisation of the ML model, where an arbitrary values of β_0 may be added. The results are qualitatively similar within each class

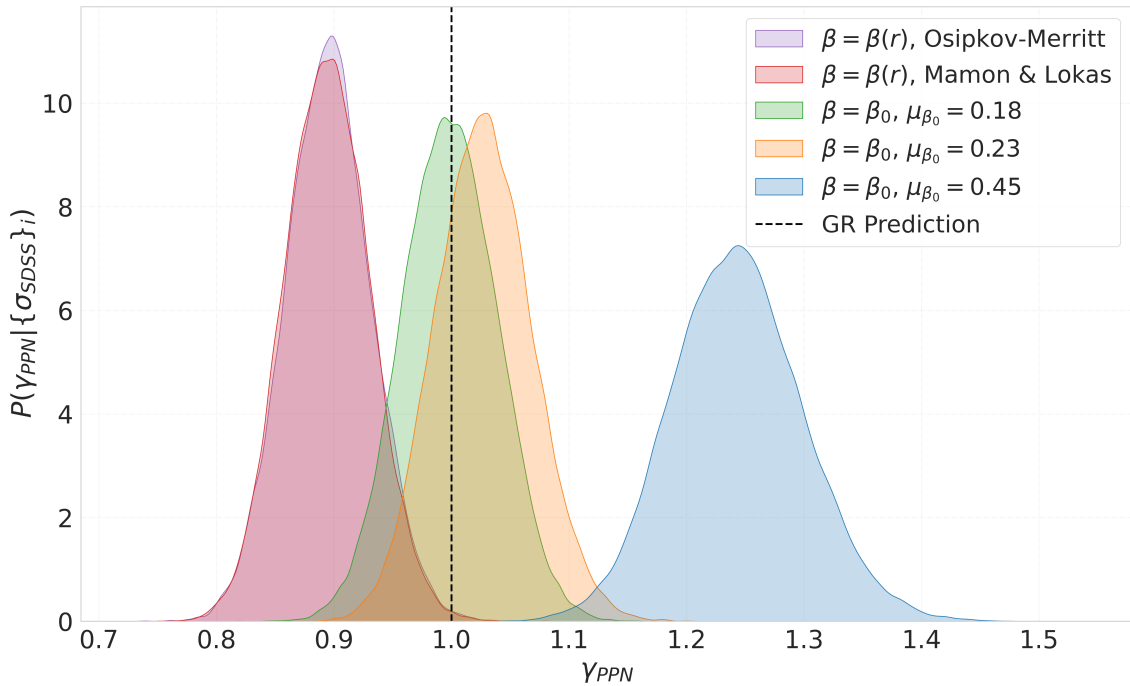


Figure 3.11: Posterior Probability Distribution of γ_{PPN} for the models leading to Gaussian-like posterior PDFs for this quantity. The first two leftmost curves, in purple and red, correspond to the models incorporating radial β profiles from Osipkov-Merritt and Mamon & Lokas, respectively. The remaining three curves represent models with a constant $\beta = \beta_0$. The first curve in green, reproduces the results of [25]. The second curve in orange, reflects the outcome when using the prior on β_0 based on the study conducted by [33]. Finally, the rightmost curve, in blue, represents the results obtained using the $P(\beta_0)$ based on measurements from [53]. The dashed black line represents the predicted value for the General Relativity case, $\gamma_{PPN} = 1$.

From the aforementioned sets of models and prior, five of them yielded Gaussian-like PDFs for the PPN parameter. For these cases, it becomes possible to obtain a good estimation for the mean γ_{PPN} and its dispersion ε_γ , by fitting a Gaussian function to the PDF. These posteriors are shown in Figure 3.11, where the dashed black line in this plot represents the predicted value for the General Relativity case, $\gamma_{PPN} = 1$. The first two leftmost curves, in purple and red, correspond to the models incorporating radial β profiles from Osipkov-Merritt (OM) and Mamon & Lokas (ML) respectively. For the OM model we obtained $\langle \gamma_{PPN,OM} \rangle = 0.896 \pm 0.035$, while for the ML profile yielded $\langle \gamma_{PPN,ML} \rangle = 0.898 \pm 0.037$. Therefore, the models in this class tend to prefer values of γ_{PPN} lower than 1.

The three curves in the right represent models with a constant β . The first curve, in green, reproduces the results of [25], where the Gaussian prior $\beta_0 = 0.18 \pm 0.13$ was employed. By fitting a Gaussian profile in the PPN parameter posterior we obtained $\gamma_{PPN,0} = 0.998 \pm 0.041$, consistent with the value reported by [25], $\gamma_{PPN} = 0.995 \pm 0.042$. The second curve, in orange, reflects the outcome when using the prior $\beta_0 = 0.23 \pm 0.19$. Fitting a Gaussian to the posterior of the PPN parameter we derived $\langle \gamma_{PPN,0} \rangle = 1.026 \pm 0.041$. Lastly, the rightmost curve, in blue, represents the results obtained using $\beta_0 = 0.45 \pm 0.25$. For this case, fitting the posterior of the PPN parameter yielded $\langle \gamma_{PPN,0} \rangle = 1.241 \pm 0.55$. we see that models with constant β tend to prefer values of γ_{PPN} close to 1 or higher depending on the prior used.

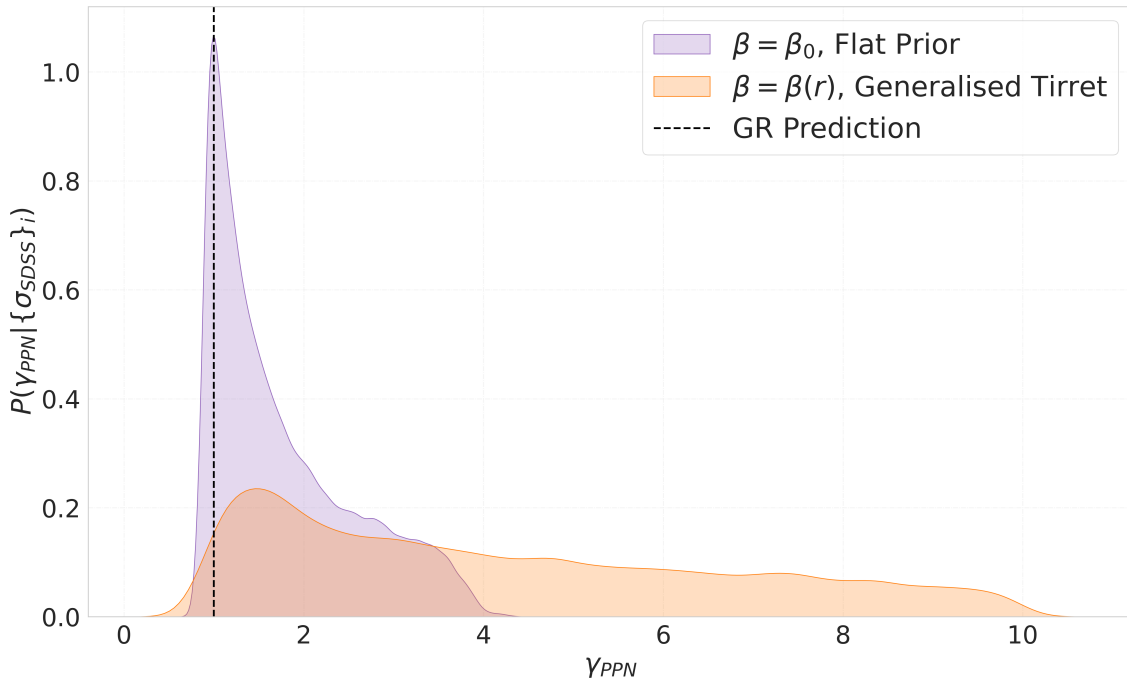


Figure 3.12: Posterior Probability Distribution for γ_{PPN} , for the models that yield a broad and skewed posterior for this parameter. The curve in purple is the result for $\beta = \beta_0$ and a flat prior on β_0 . The curve in orange is the result obtained by using the Generalised Turret model. The dashed black line correspond to $\gamma_{PPN} = 1$.

Figure 3.12 displays the two cases for which the PDF of γ_{PPN} has a broad and skewed shape, so that the constraints on γ_{PPN} are very broad. In any case, the PDF have a clear peak. The purple curve represents the case in which the anisotropy parameter was considered constant ($\beta = \beta_0$) and a flat prior bonded by $[0, 1]$ is assumed for β_0 . The value that maximise this curve is $\gamma_{PPN,0} = 1.01_{-0.14}^{+1.03}$. The orange curve is the result obtained whit the generalised Tirtet model. This PDF has an even larger spread when compared to the previous case, but it still presents a clear peak at $\gamma_{PPN,GT} = 1.47_{-0.56}^{+4.08}$. The uncertainties presented above where calculated by considering the 1σ interval.

To compare the goodness of fit of each model to the data presented in Section 3.1, we calculated the χ^2 and the χ_{red}^2 using Equations (2.29) and (2.30) respectively. The results are presented in Table 3.2. The first column indicates the model, the second column shows the corresponding χ^2 value computed at the maximum of the posterior for the parameters with flat priors, the third column displays the number of free parameters k , defined here as those with flat priors, for each model, and the last column presents the χ_{red}^2 value.

β Model	χ^2	k	χ_{red}^2
$\beta_0 = 0.18 \pm 0.13$	186.19	1	2.36
$\beta_0 = 0.45 \pm 0.25$	186.33	1	2.36
$\beta_0 = 0.23 \pm 0.19$	186.25	1	2.36
Flat $P(\beta_0)$	186.28	2	2.39
Mamon & Lokas	186.61	2	2.39
Osipkov-Merritt	186.68	2	2.39
Generalised Tirret	186.62	3	2.42

Table 3.2: This table displays the values of χ^2 and χ_{red}^2 for each model.

The results in Table 3.2 are organised according to the different classes of models considered. The first set of results corresponds to the model class in which β is equal to a constant value β_0 . Following that, we present the results for the second class of models where β has a radial dependence, with $\beta(r = 0) = 0$ and $\beta(r \rightarrow \infty)$ approaching an asymptotic value. Finally, the last line in the table represents the generalisation of the ML model, with $\beta(r = 0) = \beta_0$. Notably, the χ^2 values are quite similar for all models, indicating that they all provide similar fits to the data¹. However, the χ_{red}^2 values differ due to the penalty imposed by the number of free parameters. Therefore, models with an equal number of parameters can be considered equivalent among themselves. In brief, we do not see that the models with more parameters

¹It may seem strange that models with more free parameters provide a slightly worse χ^2 than models with less parameters. However, we note that, for simplicity, the χ^2 is being computed using the mode of the priors for the parameter with Gaussian priors. In other words, we are not minimising the χ^2 as a function of all parameter, but only as a function of the parameters with flat priors, setting the other parameters at the peak of their individual prior.

provide a better fit to the data.

A relevant question to ask is whether the current data provide evidence either in favour or against any of the considered models. To address this question we compute the Bayesian Information Criteria (BIC) for each model, as indicated by Equation (2.31). The corresponding results are presented in Table 3.3. The first column denotes the model, the second column shows the BIC value, and the third column displays the ΔBIC . The ΔBIC represents the difference between the BIC values of two models and is used to assess the evidence in favour of a particular model. In this study, we adopt the model used by [25] as the null hypothesis and calculate the ΔBIC for the other models.

β Model	BIC	ΔBIC
$\beta_0 = 0.18 \pm 0.13$	190.58	0
$\beta_0 = 0.45 \pm 0.25$	190.71	0.14
$\beta_0 = 0.23 \pm 0.19$	190.63	0.058
Flat $P(\beta_0)$	195.04	4.47
Mamon & Lokas	195.37	4.80
Osipkov-Merritt	195.44	4.87
Generalised Tirret	199.77	9.20

Table 3.3: The Bayesian Information Criterion for each model, as well the ΔBIC when taking the model used by [25] as null hypothesis.

Similarly to the previous table, the results in Table 3.3 are organised according to the different classes of models considered. The values of ΔBIC are commonly used to assess the evidence of one model against another, where $\Delta\text{BIC} > 5$, represents that there is strong evidence against the model with the highest criterion value, and $\Delta\text{BIC} > 10$, represents that the evidence decisively favours the model with lowest BIC (see reference [63]). Based on this criterion, the first three models (with Gaussian priors in β_0) exhibit no evidence in favour of one over the other. The subsequent three models face weak evidence against them, while the last model encounters strong evidence against it. In brief, the models with only one free parameter (γ_{PPN}) are equivalent in terms of the ΔBIC criterion. There is weak evidence against the models that add an extra parameter, be it β_0 or a . And there is strong evidence against the model with two extra parameters (both β_0 and a).

Chapter 4

Conclusions and Future Work

A quantitative test of General Relativity can be performed by combining strong gravitational lensing data with the dynamics of the lens galaxies to constrain the post-Newtonian parameter γ_{PPN} [23–28]. In this study, we investigate the impact of different models for the dynamics of the lensing galaxy on the constraint of γ_{PPN} , focusing specifically on the parameter β , which describes the anisotropy between the radial and tangential components of the velocity dispersion of stars in the galaxy acting as lens. Our objective was to assess whether different models on the anisotropy of the velocity dispersion influence the constraints on γ_{PPN} , and to explore the potential to simultaneously constrain both β and γ_{PPN} .

We employ the data set used in reference [25], consisting of 80 galaxy-galaxy strong lensing systems. Initially, we reproduce their results, which were obtained by assuming a constant β and constraining it with a Gaussian prior centred at $\beta_0 = 0.18 \pm 0.13$. Subsequently, we test two alternative priors for β_0 : one obtained from a study on galactic dynamics conducted by [33], resulting in $\beta_0 = 0.23 \pm 0.19$, and another based on measurements performed by [53], yielding $\beta_0 = 0.45 \pm 0.25$. Additionally, we allow β_0 to be a free parameter by imposing a flat prior on it. Furthermore, considering that the literature on galactic dynamics suggests that the anisotropy profile of early-type galaxies should be radially dependent, we test three models for the radial profiles: the Osipkov-Merritt model [36, 37] given by Equation (2.9), the Mamon & Lokas model [35] given by Equation (2.11), and the Generalized Tiritet model [38, 39] given by Equation (2.13).

The main findings of this work can be summarised as follows:

- There exists a strong correlation between γ_{PPN} and β_0 . This correlation was observed in cases where β_0 was kept constant and constrained by Gaussian priors. As the mean of the prior in β_0 increased, the mode of the resulting probability density function (PDF) shifted towards larger values of γ_{PPN} . This correlation was further confirmed in cases where β_0 was treated as a free parameter, specifically in the results obtained with a flat prior for β_0 and in the case of the Generalized Tiritet profile.

- When β_0 is treated as a free parameter with a flat prior, the posterior PDF on γ_{PPN} is no longer Gaussian. However, it still peaks at to values close to one, which is the predicted value for General Relativity.
- The PDF for β_0 tends to increase monotonically from $\beta_0 = 0$, but decrease abruptly close to 1 in the case where β is constant and close to 0.5 in the case of the GT profile. This limitation arises from the fact that the total β is constrained to be no larger than 1 by definition, as described in Equation (1.20).
- The dimensionless parameter a , which defines the characteristic radius r_a in Equation (2.1), could not be effectively constrained by this approach in any of the models that included this parameter, namely OM, ML and GT. Although the data favours high values of a (> 1.3).
- For the radial anisotropy profiles that have β_0 fixed at zero, namely OM and ML, we obtained Gaussian posterior PDF for γ_{PPN} .
- We calculated the χ^2 and χ_{red}^2 value for each model as a quantitative measure of how well they fit the data. Interestingly, we obtained values of χ_{red}^2 around 2.4 for all models considered. This provides a reasonable fit, taking into account that we are using a quite simple model for real systems which a much higher degree of complexity.
- We also calculated the Bayesian Information Criterion (BIC) and the Δ BIC, considering the model with $\beta_0 = 0.18 \pm 0.13$ as the null hypothesis. The models with β_0 constrained by a Gaussian prior showed Δ BIC values close to zero, indicating that they are similar to each other and have little to no evidence against them. The model with flat $P(\beta_0)$, as well as the models with the OM and ML profiles for anisotropy, had Δ BIC values between 4 and 5, indicating weak evidence against them. Finally, the model with the GT profile had a Δ BIC value of 9.20, indicating strong evidence against it. These BIC values arise from the fact that the χ^2 values are very similar for all the models, such that the difference in the BIC value is primarily driven by the model complexity, which is reflected in the number of free parameters.
- For the cases where γ_{PPN} could be well constrained, we performed a Gaussian fit to obtain measurements for it. Reproducing the results of [25], we obtained $\langle \gamma_{PPN,0} \rangle = 0.998 \pm 0.041$, which is consistent with the value reported by [25], $\gamma_{PPN} = 0.995 \pm 0.042$. When using the prior in β_0 based on the study conducted by [33], we derived $\langle \gamma_{PPN,0} \rangle = 1.026 \pm 0.041$. The results obtained using $P(\beta_0)$ based on measurements from [53] yielded $\langle \gamma_{PPN,0} \rangle = 1.241 \pm 0.055$. Taking these results at face value, we see that the first low constraint on β_0 yield results that are consistent with the expected value of γ_{PPN} for GR, which is

$\gamma_{PPN} = 1$, within the 1σ interval. However, the last scenario deviates significantly from the predicted value, exhibiting a difference above the 4σ level.

- For the model using the OM profile, we obtained $\langle \gamma_{PPN,OM} \rangle = 0.896 \pm 0.035$, and for the ML profile, we obtained $\langle \gamma_{PPN,ML} \rangle = 0.898 \pm 0.037$. These two models yielded a value of γ_{PPN} that is 10% lower than the expected value for GR. Given the derived error bars, this represents a deviation of about 3σ with respect to the GR result.
- Although the models with free β_0 did not result in Gaussian PDFs, they had clear peaks and boundaries. For the model with $\beta = \beta_0$ and flat $P(\beta_0)$, we obtained $\gamma_{PPN,0} = 1.01^{+1.03}_{-0.14}$. For the model with the GT profile and free β_0 , we obtained $\gamma_{PPN,GT} = 1.47^{+4.08}_{-0.56}$.

It is undeniable that the anisotropy in the velocity dispersion of the lens galaxy has a strong influence in the post-Newtonian parameter. It was necessary to set strong priors on β to determine γ_{PPN} and the results are highly dependants on these priors. Additionally, models incorporating radial dependence on the anisotropy parameter consistently yielded lower values of γ_{PPN} , below the predicted value of 1 in GR. This strong correlation between β and γ_{PPN} highlights the introduction of significant systematic errors in the measurement of γ_{PPN} due to choices in β . These conclusion raise questions regarding potential selection bias in prior choices for β in previous studies.

Furthermore, we could not effectively constraint β and γ_{PPN} simultaneously. When the dynamics were unconstrained, the resulting constraints on γ_{PPN} were weak, as were those on the anisotropy parameter a and β_0 . However, some conclusions could still be drawn. Although the posterior PDF of γ_{PPN} displayed a broad range, it exhibited a peak near one. The data disfavoured small values of a and imposed an upper limit of 1 on β .

The anisotropy parameter cannot be directly measured through observation [50]. However it can be indirectly estimated, as demonstrated in reference [53], that inferred a value for β using SL data. Additionally, N-body simulations, as seen in reference [33], allow for the study of the anisotropy profile. Therefore, further progress in the field requires additional knowledge on β , either from spatially resolved kinematical data or high resolution simulations.

Future studies can explore the effects of β models that are radially constant but depend on other galactic properties, such as mass, eccentricity, and/or redshift. Additionally, one can also explore the effects of solving the jeans equation for axisymmetric systems [32, 77]. Moreover, employing larger data sets and defining subsets based on the aforementioned properties can provide insights into the constraints on β and γ_{PPN} for each subset. Lastly, addressing different sources of systematic errors, as for example the uncertainties caused the choice of stellar templates for inferring the velocity dispersion of the lens galaxy with the spectra (see reference [29]), would enhance the robustness of the analysis.

Bibliography

- [1] A. Einstein, “Zur allgemeinen Relativitätstheorie”, *Sitzungsberichte der Königlich Preussischen Akademie der Wissenschaften zu Berlin* **1915**, 778–786.
- [2] A. Einstein, “Die Feldgleichungen der Gravitation”, *Sitzungsberichte der Königlich Preussischen Akademie der Wissenschaften zu Berlin* **1915**, 844–847.
- [3] A. Einstein, “Erklärung der Perihelionbewegung der Merkur aus der allgemeinen Relativitätstheorie”, *Sitzungsberichte der Königlich Preussischen Akademie der Wissenschaften zu Berlin* **1915**, 831–839.
- [4] A. S. Eddington, “The total eclipse of 1919 May 29 and the influence of gravitation on light”, *The Observatory* **1919**, *42*, 119–122.
- [5] C. M. Will, “The Confrontation between General Relativity and Experiment”, *Living Reviews in Relativity* **2014**, *17*, 1–117, DOI 10.12942/lrr-2014-4.
- [6] J. H. Taylor, L. A. Fowler, P. M. McCulloch, “Measurements of general relativistic effects in the binary pulsar PSR 1913+16”, *Nature* **1979**, *277*, 437–440, DOI 10.1038/277437a0.
- [7] B. Bertotti, L. Iess, P. Tortora, “A test of general relativity using radio links with the Cassini spacecraft”, *Nature* **2003**, *425*, 374–376, DOI 10.1038/nature01997.
- [8] N. Ashby, “Relativity and the Global Positioning System”, *Physics Today* **2002**, *55*, 41–47, DOI 10.1063/1.1485583.
- [9] B. P. Abbott et al., “Observation of Gravitational Waves from a Binary Black Hole Merger”, *Physical Review Letters* **2016**, *116*, 061102, DOI 10.1103/PhysRevLett.116.061102.
- [10] B. P. Abbott et al., “Tests of General Relativity with GW150914”, *Physical Review Letters* **2016**, *116*, 221101, DOI 10.1103/PhysRevLett.116.221101.
- [11] B. P. Abbott et al., “GW170817: Observation of Gravitational Waves from a Binary Neutron Star Inspiral”, *Physical Review Letters* **2017**, *119*, 161101, DOI 10.1103/PhysRevLett.119.161101.

- [12] E. H. T. Collaboration et al., “First M87 Event Horizon Telescope Results. I. The Shadow of the Supermassive Black Hole”, *The Astrophysical Journal Letters* **2019**, *875*, L1, DOI 10.3847/2041-8213/ab0ec7.
- [13] E. H. T. Collaboration et al., “First Sagittarius A* Event Horizon Telescope Results. I. The Shadow of the Supermassive Black Hole in the Center of the Milky Way”, *The Astrophysical Journal Letters* **2022**, *930*, L12, DOI 10.3847/2041-8213/ac6674.
- [14] A. G. Riess et al., “Observational evidence from supernovae for an accelerating universe and a cosmological constant”, *The Astronomical Journal* **1998**, *116*, 1009–1038, DOI 10.1086/300499.
- [15] S. Perlmutter, M. S. Turner, M. White, “Constraining dark energy with type Ia supernovae and large-scale structure”, *Physical Review Letters* **1999**, *83*, 670–673, DOI 10.1103/PhysRevLett.83.670.
- [16] L. Verde, T. Treu, A. G. Riess, “Tensions between the early and late Universe”, *Nature Astronomy* **2019**, *3*, 891–895, DOI 10.1038/s41550-019-0902-0.
- [17] V. C. Rubin, J. Ford, W. K., “Rotation of the Andromeda Nebula from a Spectroscopic Survey of Emission Regions”, *The Astrophysical Journal* **1970**, *159*, 379, DOI 10.1086/150317.
- [18] P. Schneider, *Extragalactic Astronomy and Cosmology*, Springer Berlin Heidelberg, **2006**, DOI 10.1007/978-3-540-33175-9.
- [19] B. Ryden, *Introduction to Cosmology*, Cambridge University Press, **2016**, DOI 10.1017/9781316651087.
- [20] A. Hees, A. Füzfa, “Combined cosmological and solar system constraints on chameleon mechanism”, *Physical Review D* **2012**, *85*, 103005, DOI 10.1103/PhysRevD.85.103005.
- [21] C. Burrage, J. Sakstein, “Tests of chameleon gravity”, *Living reviews in relativity* **2018**, *21*, 1–58, DOI 10.1007/s41114-018-0011-x.
- [22] H. Desmond, P. G. Ferreira, “Galaxy morphology rules out astrophysically relevant Hu-Sawicki $f(R)$ gravity”, *Physical Review D* **2020**, *102*, 104060, DOI 10.1103/PhysRevD.102.104060.
- [23] A. S. Bolton, S. Rappaport, S. Burles, “Constraint on the Post-Newtonian Parameter γ on Galactic Size Scales”, *Physical Review D* **2006**, *74*, 061501, DOI 10.1103/PhysRevD.74.061501.
- [24] J. Schwab, A. S. Bolton, S. A. Rappaport, “Galaxy-Scale Strong-Lensing Tests of Gravity and Geometric Cosmology: Constraints and Systematic Limitations”, *The Astrophysical Journal* **2010**, *708*, 750–757, DOI 10.1088/0004-637X/708/1/750.

- [25] S. Cao et al., “Test of parametrized post-Newtonian gravity with galaxy-scale strong lensing systems”, *The Astrophysical Journal* **2017**, 835, 92, DOI 10.3847/1538-4357/835/1/92.
- [26] T. E. Collett et al., “A precise extragalactic test of General Relativity”, *Science* **2018**, 360, 1342–1346, DOI 10.1126/science.aao2469.
- [27] X.-H. Liu, Z.-H. Li, J.-Z. Qi, X. Zhang, “Galaxy-Scale Test of General Relativity with Strong Gravitational Lensing”, *The Astrophysical Journal* **2022**, 927, 28, DOI 10.3847/1538-4357/ac4c3b.
- [28] J.-J. Wei, Y. Chen, S. Cao, X.-F. Wu, “Direct Estimate of the Post-Newtonian Parameter and Cosmic Curvature from Galaxy-scale Strong Gravitational Lensing”, *The Astrophysical Journal Letters* **2022**, 927, L1, DOI 10.3847/2041-8213/ac551e.
- [29] C. R. Melo-Carneiro, C. Furlanetto, A. L. Chies-Santos, “Probing general relativity in galactic scales at $z \sim 0.3$ ”, *Monthly Notices of the Royal Astronomical Society* **2023**, 520, 1613–1629, DOI 10.1093/mnras/stad162.
- [30] P. Schneider, J. Ehlers, E. E. Falco, *Gravitational Lenses*, Springer Berlin Heidelberg, **1992**, DOI 10.1007/978-3-662-03758-4.
- [31] A. J. Shajib et al., “Strong Lensing by Galaxies”, *arXiv preprint arXiv:2210.10790* **2022**.
- [32] J. Binney, S. Tremaine, *Galactic Dynamics: Second Edition*, Princeton university press, **2008**, DOI 10.2307/j.ctvc778ff.
- [33] Y. Wang et al., “Early-type galaxy density profiles from IllustrisTNG – I. Galaxy correlations and the impact of baryons”, *Monthly Notices of the Royal Astronomical Society* **2019**, 491, 5188–5215, DOI 10.1093/mnras/stz3348.
- [34] G. A. Mamon, E. L. Lokas, T. Sanchis, “Breaking the mass / anisotropy degeneracy in the Coma cluster”, *Proceedings of the International Astronomical Union* **2004**, 2004, 413–417, DOI 10.1017/S1743921304000869.
- [35] G. A. Mamon, E. L. Lokas, “Dark matter in elliptical galaxies—II. Estimating the mass within the virial radius”, *Monthly Notices of the Royal Astronomical Society* **2005**, 363, 705–722, DOI 10.1111/j.1365-2966.2005.09400.x.
- [36] L. P. Osipkov, “Spherical systems of gravitating bodies with ellipsoidal velocity distribution”, *Pisma v Astronomicheskii Zhurnal* **1979**, 5, 77–80.
- [37] D. Merritt, “Distribution functions for spherical galaxies”, *Monthly Notices of the Royal Astronomical Society* **1985**, 214, 25P–28P, DOI 10.1093/mnras/214.1.25P.

- [38] O. Tiret, F. Combes, G. W. Angus, B. Famaey, H. S. Zhao, “Velocity dispersion around ellipticals in MOND”, *Astronomy & Astrophysics* **2007**, *476*, L1–L4, DOI 10.1051/0004-6361:20078569.
- [39] Mamon, G. A. et al., “Structural and dynamical modeling of WINGS clusters - II. The orbital anisotropies of elliptical, spiral, and lenticular galaxies”, *Astronomy & Astrophysics* **2019**, *631*, A131, DOI 10.1051/0004-6361/201935081.
- [40] E. Poisson, C. M. Will, *Gravity: Newtonian, Post-Newtonian, Relativistic*, Cambridge University Press, **2014**, DOI 10.1017/cbo9781139507486.
- [41] J. D. Toniato, D. C. Rodrigues, “Post-Newtonian γ -like parameters and the gravitational slip in scalar-tensor and $f(R)$ theories”, *Physical Review D* **2021**, *104*, 044020, DOI 10.1103/PhysRevD.104.044020.
- [42] X. Zhang, W. Zhao, H. Huang, Y. Cai, “Post-Newtonian parameters and cosmological constant of screened modified gravity”, *Physical Review D* **2016**, *93*, 124003, DOI 10.1103/PhysRevD.93.124003.
- [43] J. Sakstein, “Astrophysical tests of screened modified gravity”, *International Journal of Modern Physics D* **2018**, *27*, 1848008, DOI 10.1142/s0218271818480085.
- [44] E. Bertschinger, “One gravitational potential or two? Forecasts and tests”, *Philosophical Transactions of the Royal Society of London Series A* **2011**, *369*, 4947–4961, DOI 10.1098/rsta.2011.0369.
- [45] C. M. O’Riordan, G. Despali, S. Vegetti, M. R. Lovell, Á. Moliné, “Sensitivity of strong lensing observations to dark matter substructure: a case study with Euclid”, *Monthly Notices of the Royal Astronomical Society* **2023**, *521*, 2342–2356, DOI 10.1093/mnras/stad650.
- [46] D. J. Lagattuta et al., “RXJ0437+00: constraining dark matter with exotic gravitational lenses”, *Monthly Notices of the Royal Astronomical Society* **2023**, *522*, 1091–1107, DOI 10.1093/mnras/stad803.
- [47] X. Cao et al., “Systematic Errors Induced by the Elliptical Power-law model in Galaxy-Galaxy Strong Lens Modeling”, *Research in Astronomy and Astrophysics* **2022**, *22*, 025014, DOI 10.1088/1674-4527/ac3f2b.
- [48] Y. Chen, R. Li, Y. Shu, X. Cao, “Assessing the effect of lens mass model in cosmological application with updated galaxy-scale strong gravitational lensing sample”, *Monthly Notices of the Royal Astronomical Society* **2019**, *488*, 3745–3758, DOI 10.1093/mnras/stz1902.

- [49] Y. Wang et al., “Early-type galaxy density profiles from IllustrisTNG – II. Evolutionary trend of the total density profile”, *Monthly Notices of the Royal Astronomical Society* **2019**, *490*, 5722–5738, DOI 10.1093/mnras/stz2907.
- [50] Y. Wang et al., “Early-type galaxy density profiles from IllustrisTNG – III. Effects on outer kinematic structure”, *Monthly Notices of the Royal Astronomical Society* **2022**, *513*, 6134–6151, DOI 10.1093/mnras/stac1375.
- [51] D. Xu et al., “The inner structure of early-type galaxies in the Illustris simulation”, *Monthly Notices of the Royal Astronomical Society* **2017**, *469*, 1824–1848, DOI 10.1093/mnras/stx899.
- [52] J. I. Read et al., “Breaking beta: a comparison of mass modelling methods for spherical systems”, *Monthly Notices of the Royal Astronomical Society* **2021**, *501*, 978–993, DOI 10.1093/mnras/staa3663.
- [53] L. V. E. Koopmans et al., “The Structure And Dynamics Of Massive Early-Type Galaxies: On Homology, Isothermality, And Isotropy Inside One Effective Radius”, *The Astrophysical Journal* **2009**, *703*, L51, DOI 10.1088/0004-637X/703/1/L51.
- [54] L. Ciotti, L. Morganti, P. T. De Zeeuw, “Two-component galaxies with flat rotation curve”, *Monthly Notices of the Royal Astronomical Society* **2009**, *393*, 491–500, DOI 10.1111/j.1365-2966.2008.14009.x.
- [55] P. J. Humphrey, D. A. Buote, “The slope of the mass profile and the tilt of the Fundamental Plane in early-type galaxies”, *Monthly Notices of the Royal Astronomical Society* **2010**, *403*, 2143–2151, DOI 10.1111/j.1365-2966.2010.16257.x.
- [56] S. Bellstedt et al., “The SLUGGS survey: a comparison of total-mass profiles of early-type galaxies from observations and cosmological simulations, to ~ 4 effective radii”, *Monthly Notices of the Royal Astronomical Society* **2018**, *476*, 4543–4564, DOI 10.1093/mnras/sty456.
- [57] L. Pizzuti, I. D. Saltas, L. Amendola, “MG-MAMPOSST: a code to test modifications of gravity with internal kinematics and lensing analyses of galaxy clusters”, *Monthly Notices of the Royal Astronomical Society* **2021**, *506*, 595–612, DOI 10.1093/mnras/stab1727.
- [58] J. Binney, G. A. Mamon, “M/L and velocity anisotropy from observations of spherical galaxies, or must M87 have a massive black hole?”, *Monthly Notices of the Royal Astronomical Society* **1982**, *200*, 361–375, DOI 10.1093/mnras/200.2.361.
- [59] G. M. Eadie et al., “Practical Guidance for Bayesian Inference in Astronomy”, *arXiv preprint arXiv:2302.04703* **2023**.
- [60] E. D. Feigelson, G. J. Babu, *Modern Statistical Methods for Astronomy: With R Applications*, Cambridge University Press, **2012**, DOI 10.1017/cbo9781139015653.

- [61] D. W. Scott, *Multivariate density estimation: theory, practice, and visualization*, John Wiley & Sons, **2015**, DOI 10.1002/9780470316849.
- [62] S. Baker, R. D. Cousins, “Clarification of the use of CHI-square and likelihood functions in fits to histograms”, *Nuclear Instruments and Methods in Physics Research* **1984**, 221, 437–442, DOI 10.1016/0167-5087(84)90016-4.
- [63] A. R. Liddle, “Information criteria for astrophysical model selection”, *Monthly Notices of the Royal Astronomical Society: Letters* **2007**, 377, L74–L78, DOI 10.1111/j.1745-3933.2007.00306.x.
- [64] G. Claeskens, N. L. Hjort, *Model Selection and Model Averaging*, Cambridge University Press, **2008**, DOI 10.1017/cbo9780511790485.
- [65] M. S. Talbot, J. R. Brownstein, K. S. Dawson, J.-P. Kneib, J. Bautista, “The completed SDSS-IV extended Baryon Oscillation Spectroscopic Survey: a catalogue of strong galaxy–galaxy lens candidates”, *Monthly Notices of the Royal Astronomical Society* **2021**, 502, 4617–4640, DOI 10.1093/mnras/stab267.
- [66] X. Cao et al., “LESSER: a Catalogue of Spectroscopically Selected Sample of Lyman- α Emitters Lensed by Galaxies”, *Monthly Notices of the Royal Astronomical Society* **2020**, 499, 3610–3619, DOI 10.1093/mnras/staa3058.
- [67] R. Cañameras et al., “HOLISMOKES - II. Identifying Galaxy-Scale Strong Gravitational Lenses in Pan-Starrs Using Convolutional Neural Networks”, *Astronomy & Astrophysics* **2020**, 644, A163, DOI 10.1051/0004-6361/202038219.
- [68] X. Huang et al., “Discovering New Strong Gravitational Lenses in the DESI Legacy Imaging Surveys”, *The Astrophysical Journal* **2021**, 909, 27, DOI 10.3847/1538-4357/abd62b.
- [69] S. Cao, M. Biesiada, R. Gavazzi, A. Piórkowska, Z.-H. Zhu, “Cosmology With Strong-lensing Systems”, *The Astrophysical Journal* **2015**, 806, 185, DOI 10.1088/0004-637x/806/2/185.
- [70] J. R. Brownstein et al., “The Boss Emission-line Lens Survey (Bells). I. A Large Spectroscopically Selected Sample Of Lens Galaxies At Redshift $\sim 0.5^*$ ”, *The Astrophysical Journal* **2011**, 744, 41, DOI 10.1088/0004-637x/744/1/41.
- [71] A. Sonnenfeld, R. Gavazzi, S. H. Suyu, T. Treu, P. J. Marshall, “The SL2S Galaxy-scale Lens Sample. III. Lens Models, Surface Photometry, and Stellar Masses for the Final Sample”, *The Astrophysical Journal* **2013**, 777, 97, DOI 10.1088/0004-637x/777/2/97.
- [72] A. Sonnenfeld et al., “The SL2S Galaxy-Scale Lens Sample. IV. The Dependence of the Total Mass Density Profile of Early-Type Galaxies on Redshift, Stellar Mass, and Size”, *The Astrophysical Journal* **2013**, 777, 98, DOI 10.1088/0004-637x/777/2/98.

- [73] A. S. Bolton et al., “The Sloan Lens ACS Survey. V. The Full ACS Strong-Lens Sample*”, *The Astrophysical Journal* **2008**, *682*, 964, DOI 10.1086/589327.
- [74] M. W. Auger et al., “The Sloan Lens Acs Survey. Ix. Colors, Lensing, And Stellar Masses Of Early-type Galaxies”, *The Astrophysical Journal* **2009**, *705*, 1099, DOI 10.1088/0004-637x/705/2/1099.
- [75] T. Treu, L. V. E. Koopmans, “Massive Dark Matter Halos and Evolution of Early-Type Galaxies to $z \approx 1^*$ ”, *The Astrophysical Journal* **2004**, *611*, 739, DOI 10.1086/422245.
- [76] L. V. E. Koopmans, T. Treu, “The Structure and Dynamics of Luminous and Dark Matter in the Early-Type Lens Galaxy of 0047-281 at $z = 0.485^*$ ”, *The Astrophysical Journal* **2003**, *583*, 606, DOI 10.1086/345423.
- [77] M. Cappellari, “Measuring the inclination and mass-to-light ratio of axisymmetric galaxies via anisotropic Jeans models of stellar kinematics”, *Monthly Notices of the Royal Astronomical Society* **2008**, *390*, 71–86, DOI 10.1111/j.1365-2966.2008.13754.x.
- [78] D. Kahaner, C. B. Moler, S. Nash, *Numerical Methods and Software*, Prentice-Hall, **1989**.
- [79] R. Piessens, E. de Doncker-Kapenga, C. W. Überhuber, D. K. Kahaner, *Quadpack: A subroutine package for automatic integration*, Springer Berlin, Heidelberg, **2012**, DOI 10.1007/978-3-642-61786-7.
- [80] M. Galassi, *et al*, *GNU Scientific Library: Reference Manual*, Network Theory Ltd., **2009**.
- [81] T. Hahn, “Cuba – a library for multidimensional numerical integration”, *Computer Physics Communications* **2005**, *168*, 78–95, DOI 10.1016/j.cpc.2005.01.010.

Appendix A

Numerical Integration

One of the biggest technical challenges of this work was to solve Equations (2.19) and (2.15). While these equations have exact analytical solutions for a constant β , the situation becomes more complex when considering a radial profile for β . In such cases, these equations no longer have analytically solvable solutions. This complexity arises due to the involvement of various hyper-geometrical functions, even in the case of constant β , where the analytical solution is already intricate. Incorporating radial components in β introduces additional local difficulties that cannot be overcome through simple substitutions. To tackle this problem we developed a code to numerically solve these integrals using specific libraries for this. In this Appendix we will explain this process.

Most modern integration algorithms employ an automatic adaptive approach to the Gaussian Quadrature (G_n) rule. Here n is the order of the integration rule and the precision of it depends on this order. To understand how to use G_n rule, we will consider an one-dimensional integral problem

$$I = \int_a^b f(x)dx, \quad (\text{A.1})$$

where $f(x)$ is an arbitrary function and $[a, b]$ represents the integration interval. A general solution for I can be given by

$$I = G_n + O(n), \quad (\text{A.2})$$

where $O(n)$ is the error.

The G_n rule can be given by [78]

$$G_n = \sum_{i=1}^n \omega_i f(x_i), \quad (\text{A.3})$$

where x_i are the nodes defined as a fixed value within the interval $[a, b]$, $f(x_i)$ is the function evaluated in each node, and ω_i denotes a weight for the function in that particular

node. The process of solving a integral numerical with the G_n rule involves determining the values for the nodes x_i and the corresponding weights ω_i . To accomplish this, we will follow the approach presented by [78], and expand the function $f(x)$ in a Taylor series around the midpoint m :

$$f(x) = f(m) + f'(m)(x-m) + f''(m)\frac{(x-m)^2}{2} + f'''(m)\frac{(x-m)^3}{6} + f''''(m)\frac{(x-m)^4}{24} + \dots \quad (\text{A.4})$$

Here, the midpoint is given by

$$m = \frac{b-a}{2}. \quad (\text{A.5})$$

By substituting Equation (A.4) into Equation (A.1), and solving the integral for x , we obtain

$$I = f(m)(b-a) + f''(m)\frac{(b-a)^3}{24} + f''''(m)\frac{(b-a)^5}{1920} + \dots \quad (\text{A.6})$$

It is important to notice that terms that multiply the odd derivatives will naturally become to zero, this fact can simplify the calculations.

For the next step lets consider the case of the two points Gaussian quadrature rule, for which $n = 2$, the integration rule will be denoted as G_2 and Equation (A.3) will be expressed as

$$G_2 = \omega_1 f(x_1) + \omega_2 f(x_2). \quad (\text{A.7})$$

By using Equation (A.4) we can determine the values of $f(x_1)$ and $f(x_2)$ and rewrite Equation (A.7) as:

$$G_2 = f(m)(\omega_1 + \omega_2) + f'(m)[\omega_1(x_1 - m) + \omega_2(x_2 - m)] + \dots \quad (\text{A.8})$$

Finally, we can compare Equations (A.8) and (A.6) to establish a system of equations. For instance, the term multiplying $f(m)$ has to be the same in both equations, therefore $\omega_1 + \omega_2 = (b-a)$. This allows us to determine solutions for the nodes and weights.

The aforementioned approach can be extended to any n -point Gaussian Quadrature rule. The greatest advantage of this method lies in the fact that it does not evaluate $f(x)$ directly on the integration limits $[a, b]$. In other words, this implies that while the G_n rule requires the function and its derivatives to be well-defined between a and b , it does not need to compute precisely at those boundaries. As long as the limits exist, the method can successfully operate even in open intervals.

Furthermore, an efficient numerical algorithm also needs to be automatically adaptive. In essence, the algorithm should be capable of subdividing the primary interval into smaller intervals in order to effectively address challenges within the function, for example local maxima or minima of the function. To achieve this, the algorithm must be able to internally estimate

and compute the relative error. This can be calculated as

$$E = \frac{|I - G_n|}{|I|}, \quad (\text{A.9})$$

where I is the real value of Equation (A.1) and G_n is the evaluation using n -point Gaussian Quadrature.

Nevertheless, in many cases, determining an exact value for I is often not feasible. Consequently, the strategy used by most routines is to calculate higher-order rules. To put it clearly, using G_{2n+1} yields a more accurate result for the integral compared to using G_n . Therefore, higher-order quadrature rules serve as improved approximations of the exact value. However, this methodology can be computationally expensive, as it is unlikely that G_{2n+1} and G_n share nodes and weights pairs. As a result, it will be necessary to calculate $3n + 1$ pairs. An alternative approach is to use the Gauss-Kronrod rule ($G_n K_{2n+1}$), where the integral value is determined using Equation (A.3) and the exact value is estimated to be

$$K_{2n+1} = \sum_{i=1}^n \omega_i f(x_i) + \sum_{j=1}^{n+1} \nu_j f(y_j). \quad (\text{A.10})$$

For this case the nodes and weights in the first sum are the same as those obtained for G_n , as a consequence it is only necessary to calculate $2n + 1$ pairs in total.

In adaptive algorithm the numerically estimated error should satisfy

$$E_{\text{num}} = \frac{|K_{2n+1} - G_n|}{|K_{2n+1}|} < \varepsilon_{\text{rel}}, \quad (\text{A.11})$$

where ε_{rel} is the reference error provided as input. If these conditions are not fulfilled, the interval $[a, b]$ from Equation (A.1) is subdivided into $[a, c]$ and $[c, b]$, and individual calculations of G_n and E are performed for each sub-interval. If the conditions are still not met, further subdivision is applied to the sub-interval with the higher error, leading to re-estimation of G_n and E . This iterative process continues until either the conditions are satisfied or the maximum subdivision limit is reached.

The application of these concepts to the problem at this work is not trivial, as Equations (2.19) and (2.15) can be summarised as a double integral as in

$$I = \int_0^\infty \int_R^\infty e^{-R^2/2b^2} \frac{r^{-\xi}}{\sqrt{r^2 - R^2}} \left(1 - \beta \frac{R^2}{r^2}\right) r R dr dR. \quad (\text{A.12})$$

Here, $b = D_L \tilde{\sigma}_{atm}$ is the only parameter that depends on the data. For the data set presented in Table 3.1, the histogram in Figure A.1 provides an overview of typical values assumed by b . The median value is $b = 0.006$, with a minimum value of $b = 0.003$ and a maximum value of

$b = 0.013$.

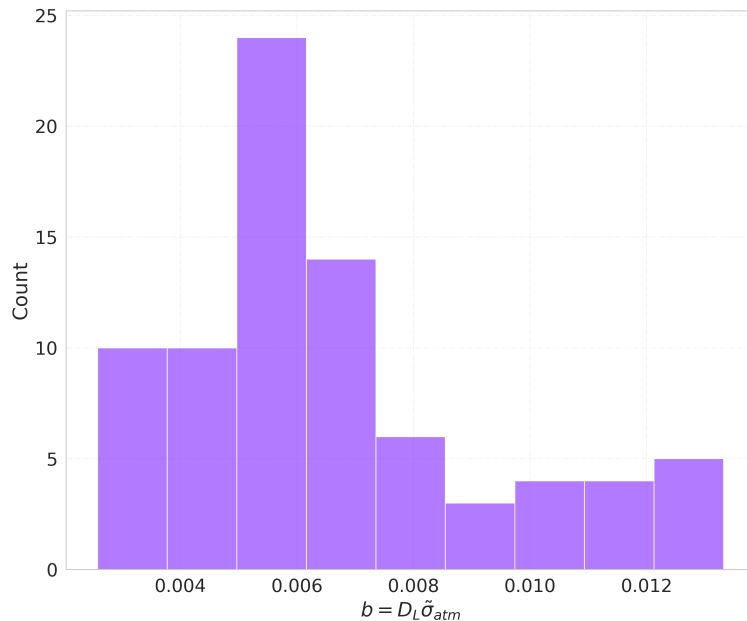


Figure A.1: Typical values for $b = D_L \tilde{\sigma}_{atm}$ in the sample from Table 3.1.

As mentioned earlier, for the case in which β is constant, Equation (A.12) has the exact solution

$$I = \frac{1}{2} \left[B \left(\frac{\xi - 1}{2}, \frac{1}{2} \right) - \beta B \left(\frac{\xi + 1}{2}, \frac{1}{2} \right) \right] (2b^2)^{(3-\xi)/2} \Gamma \left(\frac{3-\xi}{2} \right). \quad (\text{A.13})$$

Therefore, we used this case as a reference to test three routines employing two distinct approaches. The first approach involved evaluating the inner integral with a smaller tolerance, and subsequently using this result to evaluate the final integral. Two libraries were used for this approach: *scipy.integrate*¹, a Python package that employs the QAG (Quadrature Adaptive Gaussian) function from the QUADPACK library [79], which is a FORTRAN-based package for one-dimensional numerical integration, and the *GNU Scientific Library* (GSL) [80], a C language library that also provides a QAG function based on QUADPACK. The GSL pack is optimised for Cython, what make it easy to transfer the functions to python. Both aforementioned libraries employ the G₇K₁₅ rule for one-dimensional integration.

The second approach used Gaussian Cubature, which involves simultaneous evaluation of both integrals by calculating the nodes x_i and y_i within a hypercube of size h^d , where d denotes the dimension of the integral to be solved. The library employed for this approach was *Cuba* [81], specifically developed for C programming. This library also employ G₇K₁₅ rule, but extend it to the multi-dimensionnal case. To use this function in python we wrapped up the C functions into a python object.

We executed each routine using different values of ε_{rel} , specifically 10^{-1} , 10^{-2} , 10^{-3} , 10^{-4} ,

¹<https://docs.scipy.org/doc/scipy/reference/generated/scipy.integrate.dblquad.html>

10^{-5} , 10^{-6} , 10^{-7} , 10^{-8} , 10^{-9} , and 10^{-10} . Additionally, we varied the parameter b within the range of 0.002 to 0.015 for each case. By doing so, we obtained the estimated value of the integral G_n and the numerically estimated error E_{num} , which was calculated internally by the algorithm using Equation (A.11). Finally, we calculated the true relative error using Equations (A.9) and (A.13).

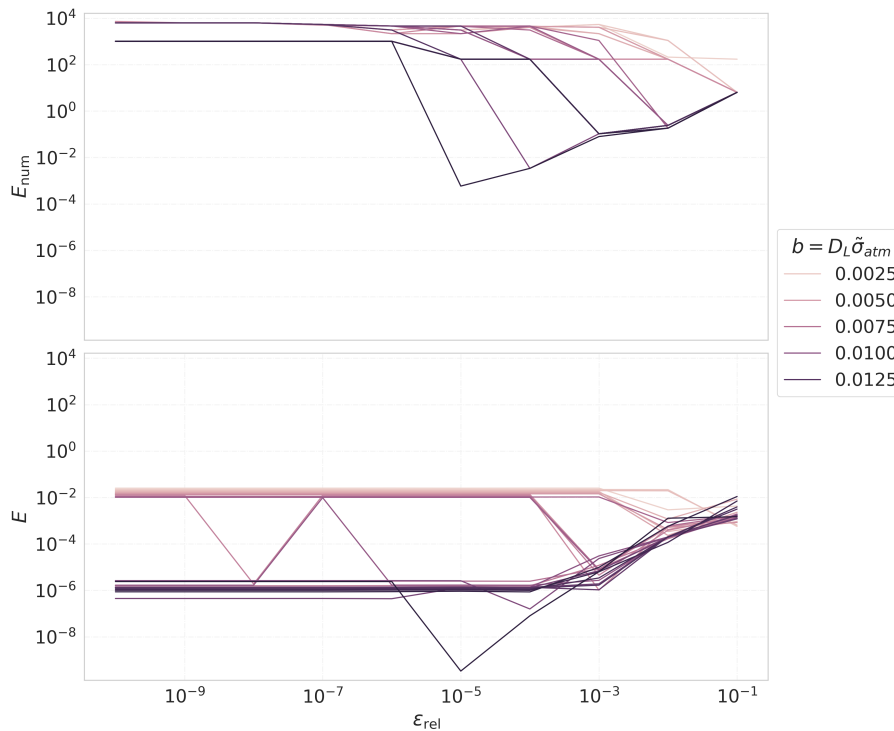


Figure A.2: Performance test for `scipy.integrate.dblquad`. The upper plot is the relative error estimated by the algorithm, while the lower plot is the true error obtained with Equations (A.9) and (A.13). Each line represents a value for $b = D_L \tilde{\sigma}_{atm}$.

Figure A.2 illustrates the performance test of the code using `scipy.integrate.dblquad` for numeric integration. The upper plot presents the algorithm's estimated relative error, while the lower plot displays the true error obtained through Equations (A.9) and (A.13). Each line corresponds to a different value of $b = D_L \tilde{\sigma}_{atm}$. Both cases exhibit oscillations, especially for larger values of ε_{rel} . In the first case, the error seems to stabilise around $\varepsilon_{\text{rel}} = 10^{-6}$, while in the second case, stabilisation occurs between $\varepsilon_{\text{rel}} = 10^{-3}$ for lower b values and $\varepsilon_{\text{rel}} = 10^{-4}$ for higher b values.

The stabilised estimated error ranges from 10^4 to 10^2 , indicating that the algorithm may not reach the error limit within the maximum number of sub-intervals. On the other hand, the true error varies between 10^{-2} and 10^{-6} . Overall, `scipy.integrate.dblquad` has two significant drawbacks. Firstly, there appears to be a clear discrepancy in the error for different values of b . This is problematic because we expect the algorithm to have consistent efficiency across the entire data set. Secondly, there is no apparent correlation between the two errors. This

discrepancy could pose a significant problem when applying the algorithm to scenarios where the true value of the integral is unknown.

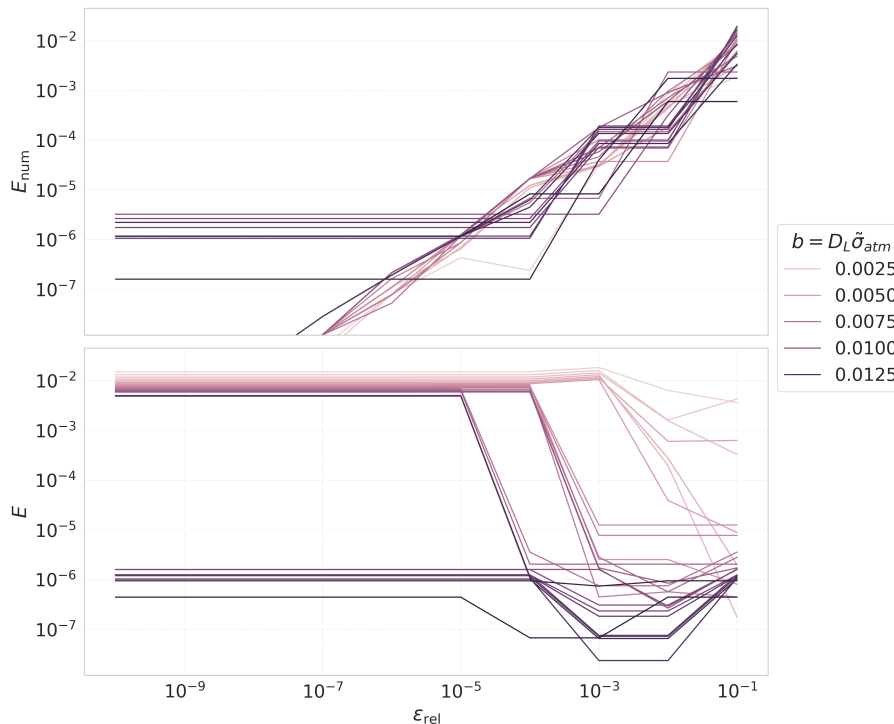


Figure A.3: Performance test for GSL. The upper plot is the relative error estimated by the algorithm, while the lower plot is the true error obtained with Equations (A.9) and (A.13). Each line represents a value for $b = D_L \tilde{\sigma}_{atm}$.

The performance test for GSL is displayed in Figure A.3. Similarly, the upper plot presents the algorithm's estimated relative error, while the lower plot displays the true error. In this case, the numerically estimated error exhibits a behaviour that is closer to what we would expect. The error decreases with ε_{rel} until the algorithm saturates. However, the true error still shows significant oscillation for higher ε_{rel} , eventually stabilising at $\varepsilon_{rel} = 10^{-3}$ for lower b values, $\varepsilon_{rel} = 10^{-4}$ for medium b values, and $\varepsilon_{rel} = 10^{-5}$ for higher b values.

The stabilised estimated error ranges from 10^{-5} to 10^{-7} , while the true error continues to vary between 10^{-2} and 10^{-6} . This observation is concerning as the estimated error is expected to be overestimated rather than underestimated [78]. Additionally, there is still no apparent correlation between the two errors, which will complicate the application of this algorithm to functions where we lack the true value.

Figure A.4 illustrates the performance of the algorithm for numeric integration using *Cuba*. The upper plot presents the algorithm's estimated relative error, while the lower plot displays the true error. These errors finally exhibit the expected behaviour, they monotonically decrease with ε_{rel} until the algorithm saturates at $\varepsilon_{rel} = 10^{-4}$. The stabilised estimated error is around 10^{-4} , whereas the true error is approximately 10^{-5} . The discrepancy in error values across b

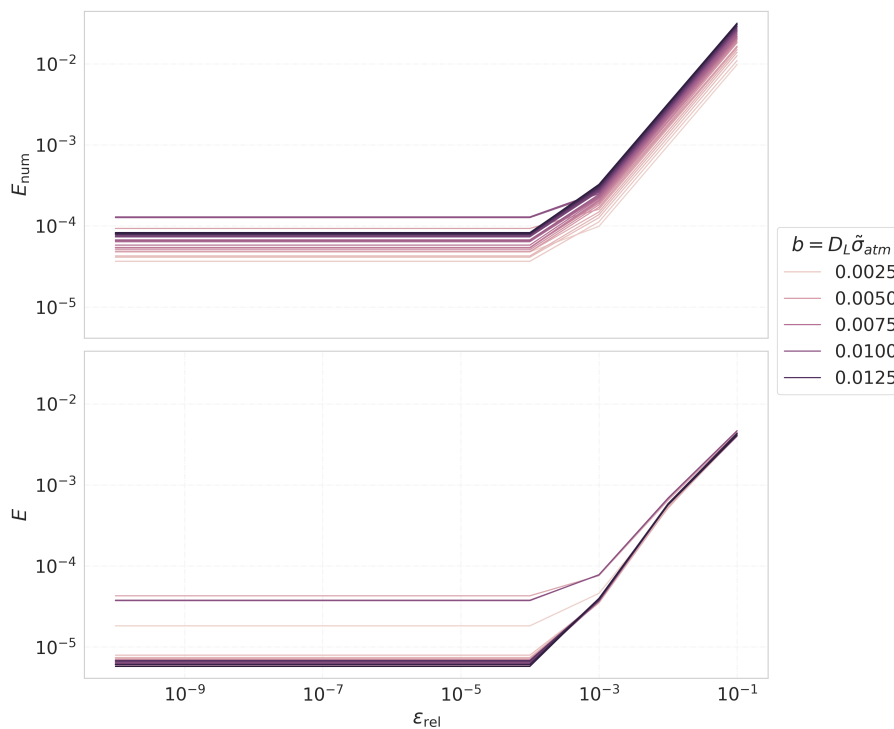


Figure A.4: Performance test for *Cuba*. The upper plot is the relative error estimated by the algorithm, while the lower plot is the true error obtained with Equations (A.9) and (A.13). Each line represents a value for $b = D_L \tilde{\sigma}_{atm}$.

is negligible. Moreover, both errors exhibit similar behaviour, making the estimated error a metric more trustworthy to evaluate the integral of functions for which we do not have the true value.

In Figure A.5, we compare the true errors for each routine. These errors were calculated using the estimated integral result for various values of b , with $\varepsilon_{rel} = 10^{-4}$, and employing Equations (A.9) and (A.13). The green histogram represents the true errors calculated for the results obtained using *scipy.integrate.dblquad*, the orange histogram represents the true error calculated for the results obtained using GSL, and the purple histogram represents the error when utilising *Cuba*.

It is evident that the error from *scipy.integrate.dblquad* exhibits a larger spread, with the values of E surpassing 0.020. When GSL is used, there is an improvement, as the relative error remains below 0.015. However, the most significant improvement is observed when using *Cuba*, where the relative errors are smaller than 0.001. Therefore, this was the routine chosen to develop the software used in this work.

In Figure A.6, the execution time test for all three tested routines is presented. The test was performed using the Python module *timeit* to run each routine 100 times for each value of ε_{rel} , with a fixed value of $b = 0.06$. The green dotted line represents the execution time for *scipy.integrate.dblquad*, the orange dashed line corresponds to the execution time for GSL,

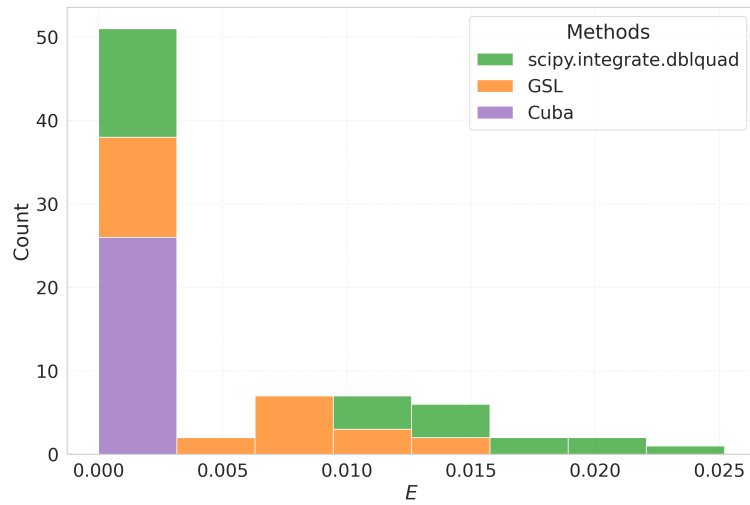


Figure A.5: Comparison of true errors across different routines for numerical integration. The green histogram represent the true errors calculated for the results obtained using *scipy.integrate.dblquad*, the orange histogram represents the true error calculated for the results obtained using GSL, and the purple histogram represents the error when making use of *Cuba*.

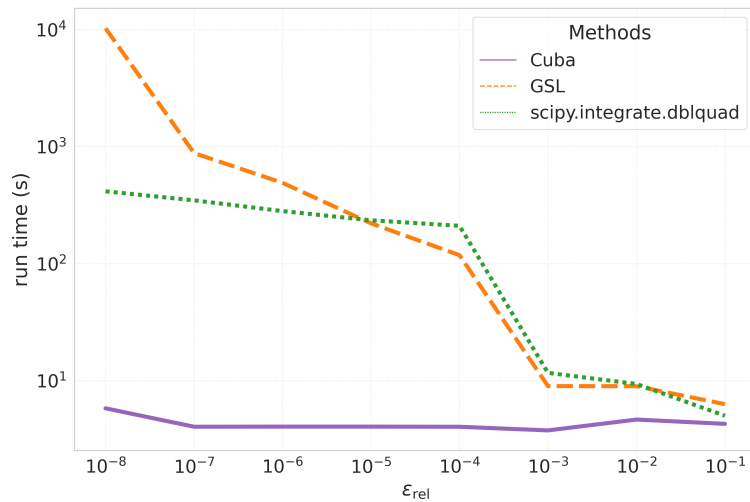


Figure A.6: Execution time test per ϵ_{rel} . The green dotted line represents the run time of the *scipy.integrate.dblquad* algorithm, the orange dashed line indicates the integration time with GSL, and the purple solid line corresponds to the run time of the *Cuba* algorithm. Each routine was executed 100 times for comprehensive analysis.

and the purple solid line is the execution time for *Cuba*. This test has demonstrated that by choosing *Cuba*, we not only improve the accuracy of the integration algorithm but also achieve a considerable gain in run time.

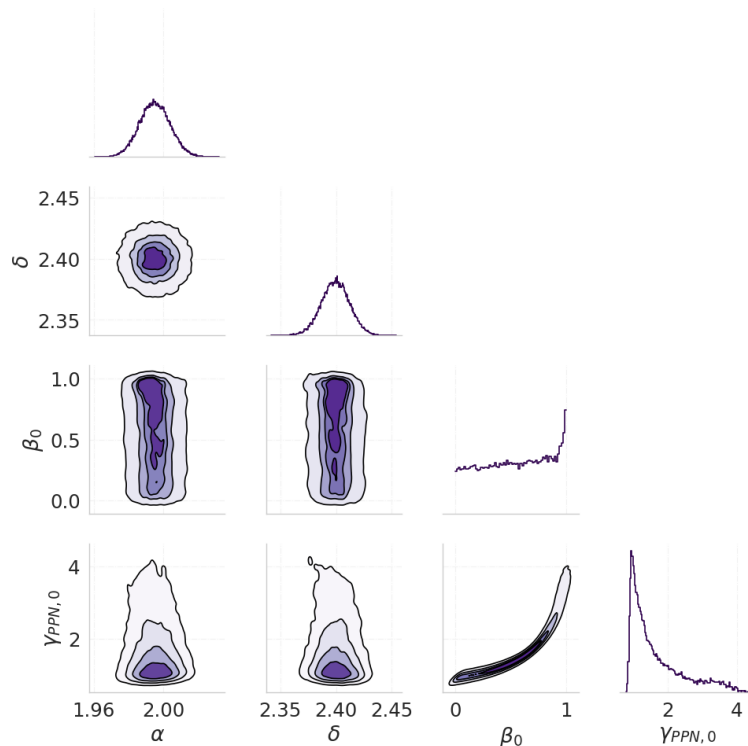


Figure A.7: Corner plot with the result for the Markov Chain Monte Carlo, for the model with β constant and with flat $P(\beta_0)$. For this case it was used a numerical integration code to obtain $\langle \sigma_{LOS,0}^2 \rangle$.

After selecting the integration method, we replicated the results for a constant β with a flat prior in β_0 . Figure 3.3 displays the outcome obtained using the exact solution for $\langle \sigma_{LOS,0}^2 \rangle$, as given by Equation (2.21). Conversely, Figure A.7 reproduces this result by employing the *Cuba* routine for numerically integrating $\langle \sigma_{LOS,0}^2 \rangle$. Both figures exhibit qualitatively equivalent results, with the only difference being some statistical fluctuations observed in Figure A.7. These fluctuations arise due to the reduced number of steps in the Markov Chain for this particular case, which is a consequence of the computational cost. This test has validated our code and has given us confidence in implementing it for models with radial anisotropy profiles, where we cannot obtain $\langle \sigma_{LOS}^2 \rangle$ analytically.